Title: Environment-independent distribution of mutational effects emerges from microscopic epistasis

Authors: Sarah Ardell[1,*], Alena Martsul[1,*,†], Milo S. Johnson[2,3], Sergey Kryazhimskiy[1,‡]

Affiliations:

[1]Department of Ecology, Behavior and Evolution, University of California San Diego, La Jolla, CA 92093

[2]Department of Integrative Biology, University of California Berkeley, Berkeley, CA 94720

[3]Biological Systems and Engineering Division, Lawrence Berkeley National Laboratory, Berkeley, CA, USA.

[*]Equal contribution

[†]Current affiliation: Platform Reagent Development Group, Illumina Inc., San Diego, CA 92122

[‡]Corresponding author: skryazhi@ucsd.edu

One Sentence Summary: The effects of mutations on microbial growth rate follow a pattern of global epistasis that is invariant across environments.

Abstract:

Predicting how new mutations alter phenotypes is difficult because mutational effects vary across genotypes and environments. Recently discovered global epistasis, where the fitness effects of mutations scale with the fitness of the background genotype, can improve predictions, but how the environment modulates this scaling is unknown. We measured the fitness effects of ~100 insertion mutations in 42 strains of *Saccharomyces cerevisiae* in six laboratory environments and found that the global-epistasis scaling is nearly invariant across environments. Instead, the environment tunes one global parameter, the background fitness at which most mutations switch sign. As a consequence, the distribution of mutational effects is remarkably predictable across genotypes and environments. Our results suggest that the effective dimensionality of genotype-to-phenotype maps across environments is surprisingly low.

Main Text:

Adaptive evolution can lead to profound changes in the phenotypes and behaviors of biological systems, sometimes with adverse and sometimes with beneficial consequences for human health, agriculture and industry (*1*–*5*). However, predicting these changes remains difficult (*6*, *7*). One major challenge is that how new mutations alter phenotypes and fitness of organisms often depends on the genetic background in which they arise (G×G interactions or "epistasis"), the environment (G×E interactions), or both (G×G×E interactions) (*8*). These interactions can alter not only the magnitude but also the sign of mutational effects, causing evolutionary trajectories to become contingent on the initial genotype, environment and random events (*9*–*11*).

Much of prior empirical work measured the effects of individual mutations on fitness-related phenotypes and characterized how these effects vary across genetic backgrounds and environments (*9*, *12*–*21*). These studies of "microscopic" G×G, G×E and G×G×E interactions provide important insights into the structure of empirical fitness landscapes and their evolutionary navigability (*22*–*24*). However, predicting evolution at the genetic level using this approach is difficult because the number of potential interactions grows super-exponentially with the number of variable loci (*25*–*27*). Predicting evolution at the phenotypic level may be more feasible and in many cases more useful (*27*, *28*). Such predictions rely on coarse-grained, or "macroscopic" descriptions of G×G, G×E and G×G×E interactions that inform us about how the distributions of mutational effects change across genotypes and environments (*22*, *29*–*31*). While the distributions of effects of mutations on fitness, or "DFEs", have been measured in many systems (*32*–*35*), we lack a systematic understanding of how DFEs vary across genetic backgrounds and environments (*31*, *36*).

Several recent studies have shown that many mutations tend to make the phenotype of an organism in which they occur less extreme (*13*, *37*–*46*), an instance of a more general phenomenon of "global epistasis" (*8*, *47*). Global epistasis is expected to arise for complex traits, including fitness (*48*), and it can be used to quantitatively predict the effects of individual mutations in new genetic backgrounds without the full knowledge of microscopic G×G interactions, thereby alleviating the combinatorial problem mentioned above (*47*, *48*). More importantly, if most mutations exhibit global epistasis, the distributions of their phenotypic effects should also have a quantitatively predictable shape (*48*), which could facilitate evolutionary predictions at the phenotypic level. However, as the variation in these distributions remains poorly characterized, no attempt has been made so far to link macroscopic G×G, G×E and G×G×E interactions to the underlying models of microscopic global epistasis.

Probing whether global epistasis models can capture G×G, G×E and G×G×E interactions at both microscopic and macroscopic levels hinges on measuring the effects of many mutations across multiple genetic backgrounds and environments. To this end, we measured how ~100 quasi-random barcoded insertion mutations constructed in our previous study (*42*) affect growth rate in

42 "background" strains of yeast *Saccharomyces cerevisiae* in six conditions (see Methods). All background genotypes are segregants from a cross between two strains of yeast (RM, a vineyard strain, and BY, a lab strain) and differ from each other by ~2×10^4 SNPs throughout the genome (*49*). Our environments varied by temperature (30°C and 37°C) and pH (3.2, 5.0 and 7.0), two stressors with global effects on yeast physiology (*50–52*), in a factorial design (see Methods, Figure S1). pH 3.2 and pH 7.0 are close to the lower and upper end of the viability range of our strains whereas both temperatures are well within the viability range. This choice of environments allowed us to explore a different (lower) range of growth rates of the background strains than in previous studies. Unlike previous studies, we kept our cultures growing close to the exponential steady state, which enabled us to infer the effect of each insertion mutation on absolute growth rate (GR, denoted by λ) from bulk barcode-based competition experiments, with precision of about 6.3×10^{-3} h^{-1} (Methods).

We first estimated the effects of our mutations on GR in different background strains and environments. To this end, following Johnson et al (*42*), we designated a set of five mutations as a putatively neutral reference and found that the remaining 94 mutations exhibit a range of effects on GR relative to this reference, from decreasing it by $\Delta\lambda = 0.18$ h^{-1} to increasing it by $\Delta\lambda = 0.13$ h^{-1}, with the median effect $\Delta\lambda \approx 0$ h^{-1}. We validated a subset of these estimates with an independent low-throughput competition assay (Methods; Figure S2). We then classified each mutation in each strain and environment as either beneficial or deleterious if the 99% confidence interval around its estimated effect ($\Delta\lambda$) did not overlap zero (Methods). All other mutations were classified as neutral. This procedure yielded conservative calls of mutation sign, with a false discovery rate of 2.5%.

We found that the fraction of beneficial and deleterious mutations varied between 0% and 54% and between 0 and 62% per strain, respectively. However, no single mutation was identified as either beneficial, deleterious or neutral in all strains and environments. 94% (88/94) of our mutations are beneficial in at least one strain and condition, and, of those, 98% (86/88) are also deleterious in at least one strain and condition. Even within the same environment, between 33% (31/94) and 65% (61/94) of all mutations change sign across background strains, and between 10% and 39% of mutations change sign across environments in the same strain (Figure S3). Thus, the vast majority of mutations neither unconditionally increase nor unconditionally decrease GR across genetic backgrounds and environments.

A recent global epistasis model suggests that the effects of most mutations on GR should linearly decline with the GR of the background genotype (*48*). One striking qualitative prediction of this model is that the proportion of beneficial mutations should decline with the fitness of the background strain whereas the proportion of deleterious mutations should increase. While several previous studies found evidence for global epistasis (*13*, *37–46*), none of them has observed sufficient numbers of mutational sign changes. Thus, we tested this qualitative prediction by looking for a correlation between strain GR and the proportion of mutations identified as beneficial and deleterious in that background. Consistent with the theory, we find

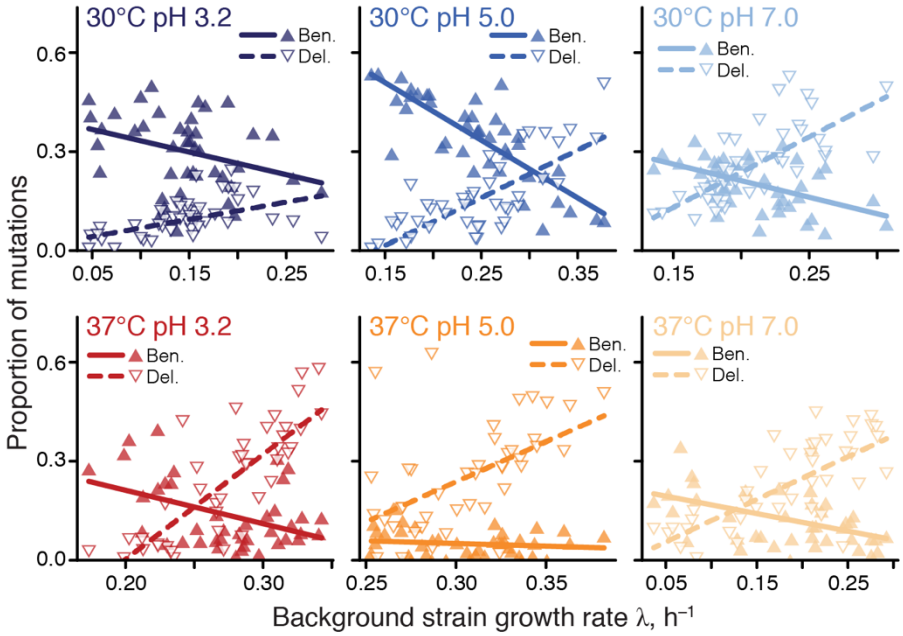

Figure 1. Proportions of beneficial and deleterious mutations vary with strain growth rate. Filled and empty triangles show the proportions of beneficial and deleterious mutations in each background strain as a function of its growth rate. Lines are the best-fit linear regressions; all are statistically significant ($P < 0.05$, t-test) except for beneficial mutations in 37°C pH 5.0.

that the proportion of beneficial and deleterious mutations decline and increase with background GR, respectively (Figure 1), and these relationships are statistically significant in all cases but one (beneficial mutations at 37°C pH 5). Thus, global epistasis is indeed a major determinant of the sign of mutations in all our environments (Figure S3C).

To probe the microscopic global epistasis model quantitatively, we modeled the effect $\Delta\lambda_{mge}$ of each mutation m on GR in strain g and environment e as

$$\Delta\lambda_{mge} = a_{me} + b_{me}\,\lambda_{ge} + \xi_{mge}, \qquad [1]$$

where λ_{ge} is the growth rate of the background genotype g and environment e. The first two terms in equation (1) capture global epistasis, a deterministic component which can be used for prediction, and ξ_{ige} captures the remaining (unpredictable) epistasis, which we refer to as "idiosyncratic" (*8*, *39*).

We found that the linear model (1) was statistically significant for 94% (88/94) of mutations (F-test, $P < 0.05$ after Benjamini-Hochberg correction), and explained on average 46% (interquartile interval [35%, 60%]) of variance in the effects of mutations across background strains and environments (Methods). When tested individually, 38% (205/545) of global epistasis slopes b_{ie} are significantly different from zero (t-test, $P < 0.05$ after Benjamini-Hochberg correction), with 98% (200/205) of them being negative (Figure 2A), consistent with the global epistasis theory (*48*) and previous observations (*39*, *42*). 96% (196/205) of significant intercepts a_{ie} are positive (Figure 2B), implying that most mutations are expected to increase GR in a hypothetical non-growing strain, which is consistent with the relationship between background GR and the proportions of beneficial and deleterious mutations observed in Figure 1.

We next sought to understand how the global epistasis slopes b_{ie} and intercepts a_{ie} vary across mutations and environments. We found that distributions of slopes are nearly invariant across

environments (Figures 2A, S4A and Table S1), whereas the distributions of intercepts vary across environments (Figure 2B, S4A and Table S1). Furthermore, slopes and intercepts are strongly negatively correlated (Figure 2C, S4), such that mutations with a zero slope have on average a zero intercept, which explains the paucity of unconditionally deleterious and beneficial mutations noted above. This relationship further implies that the global epistasis intercepts can be expressed as $a_{me} = -\bar{\lambda}_e b_{me} + \eta_{me}$. Here, the environment-specific regression coefficient $\bar{\lambda}_e$ has a clear biological interpretation: it is the "pivot GR" at which a typical mutation switches its sign (Methods). The terms η_{me}, which we refer to as the "pivot noise", can be modeled as normal random variables with zero mean and the same variance across all environments (Figure S4B).

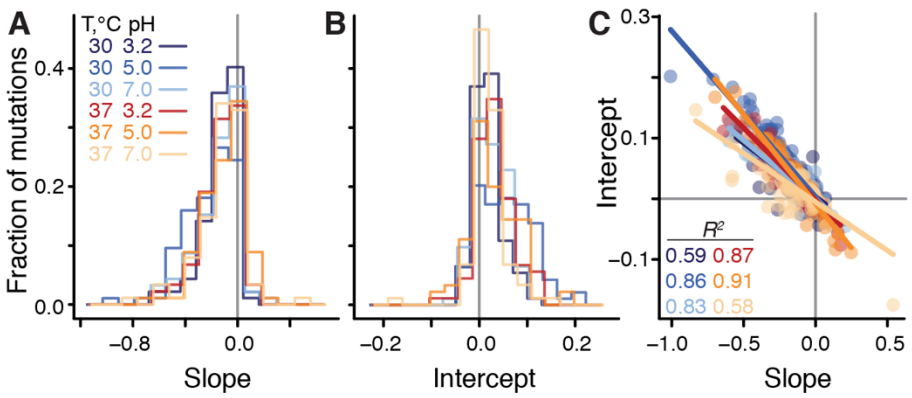

Figure 2: Distributions of global-epistasis slopes and intercepts and their correlation. A. Distributions of slopes from fitting Eq. (1) to data are largely indistinguishable between environments (see Figure S4 for statistical tests). **B.** Distributions of intercepts vary across environments (see Figure S4 for statistical tests). **C.** Correlation between slopes and intercepts. Each point represents a mutation, colored by environment. Lines are the best fit linear regressions ($P < 0.01$ for all, t-test).

We next sought to understand why the distributions of global epistasis slopes are nearly invariant across environments. We found that this near-invariance arises because of the near-invariance of slopes of individual mutations. Indeed, slopes of individual mutations are statistically indistinguishable across environments in 86% (1153/1333) of pairwise comparisons (Figures 3, S4, S5), and 56% (53/94) of mutations have statistically indistinguishable slopes in all environments. Moreover, even when slopes are statistically distinguishable, they are very similar, so that a model with six environment-specific slopes b_{ie} explains only 4% more variance in the effects of mutations compared to an "invariant slope" model where each mutation is characterized by a single environment-independent slope b_m (46% versus 42% on average). The near-invariance of global-epistasis slopes of individual mutations could arise trivially if each environment shifted the GRs of all strains by the same amount while preserving the relative order of their GRs and the effects of mutations. However, this is not the case. Slopes are nearly preserved despite the fact that the relative rank orders of background strains and mutations are reshuffled across environments (Figures S6, S7).

Taken together, the near-invariance of global-epistasis slopes across environments and the linear relationship between slopes and intercepts indicate that the microscopic G×G, G×E, and G×G×E interactions for most of our mutations are largely captured by a simplified version of equation (1),

$$\Delta\lambda_{mge} = b_m\,(\lambda_{ge} - \bar{\lambda}_e) + \zeta_{mge}, \qquad [2]$$

where $\zeta_{mge} = \eta_{me} + \xi_{mge}$. Equation (2), which we refer to as the "generalized global epistasis equation", shows that the effect of the environment on global epistasis is captured by a single effective parameter, the pivot growth rate $\bar{\lambda}_e$.

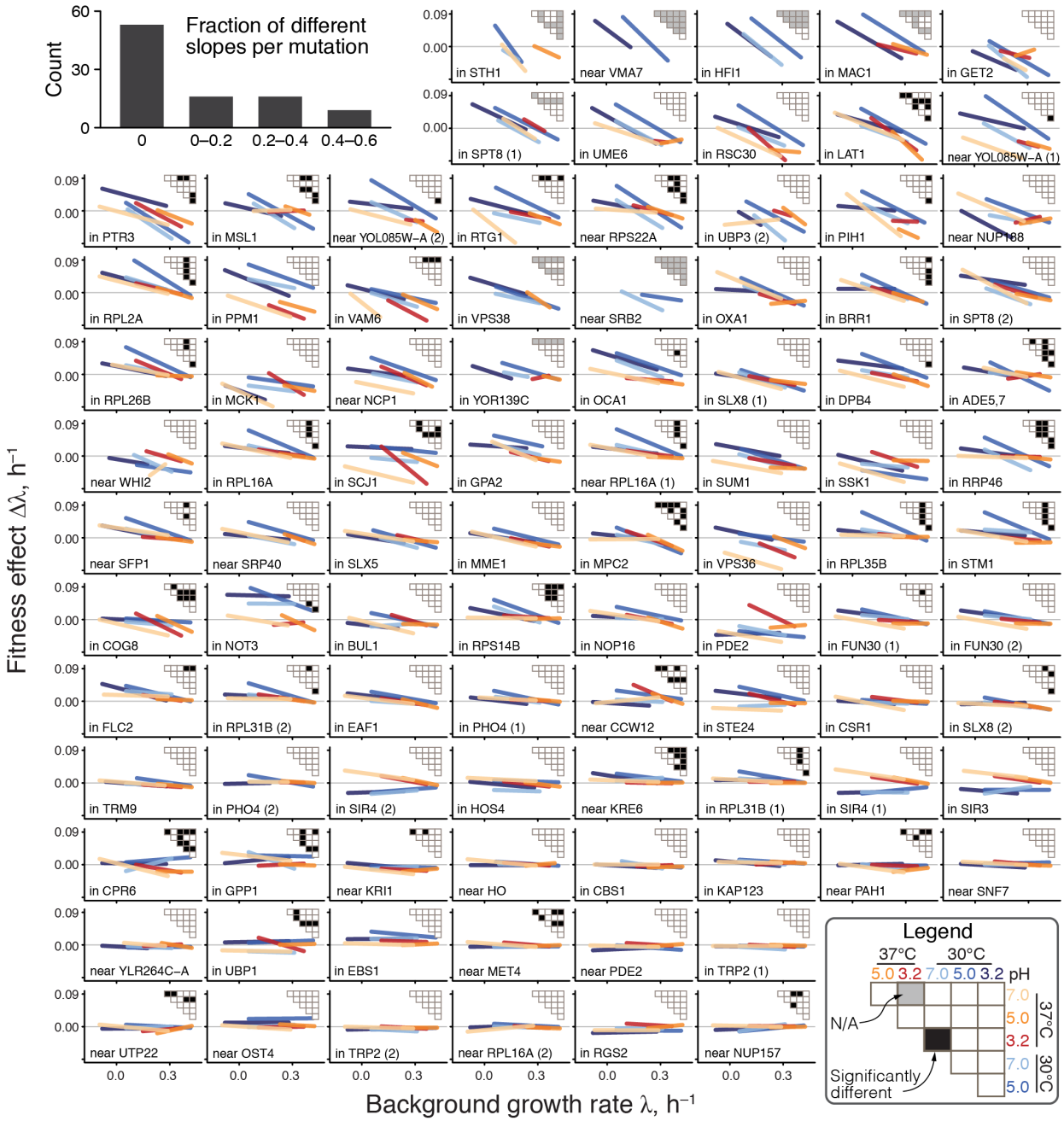

Figure 3. Global-epistasis slopes mutations are nearly invariant across environments. Panels show regression lines from fitting Eq. (1) for each mutation, colored by the environment as in previous figures. Mutations are displayed in the order of increasing mean slope. Insets show the results of all pairwise slope-comparison tests (legend in lower right). Histogram in top left shows the overall distribution of the fraction of significant test per mutation (see Methods for details).

To understand the implications of equation (2) for the macroscopic G×G, G×E and G×G×E interactions, we calculated the first three moments of the distribution of fitness effects of mutations (DFE) under the simplifying assumption that pivot noise η_{me} and idiosyncratic epistasis ξ_{me} terms are all independent (see Methods for details). As expected, the generalized global epistasis equation predicts that the DFE mean ought to decline linearly with the background GR, such that this line has a slope invariant across environments and crosses zero at the environment-specific pivot GR $\bar{\lambda}_e$.

The behavior of higher moments of the DFE is less obvious. We find that the DFE variance is predicted to depend on λ_{ge} quadratically, with the parabola's minimum achieved at the pivot GR.

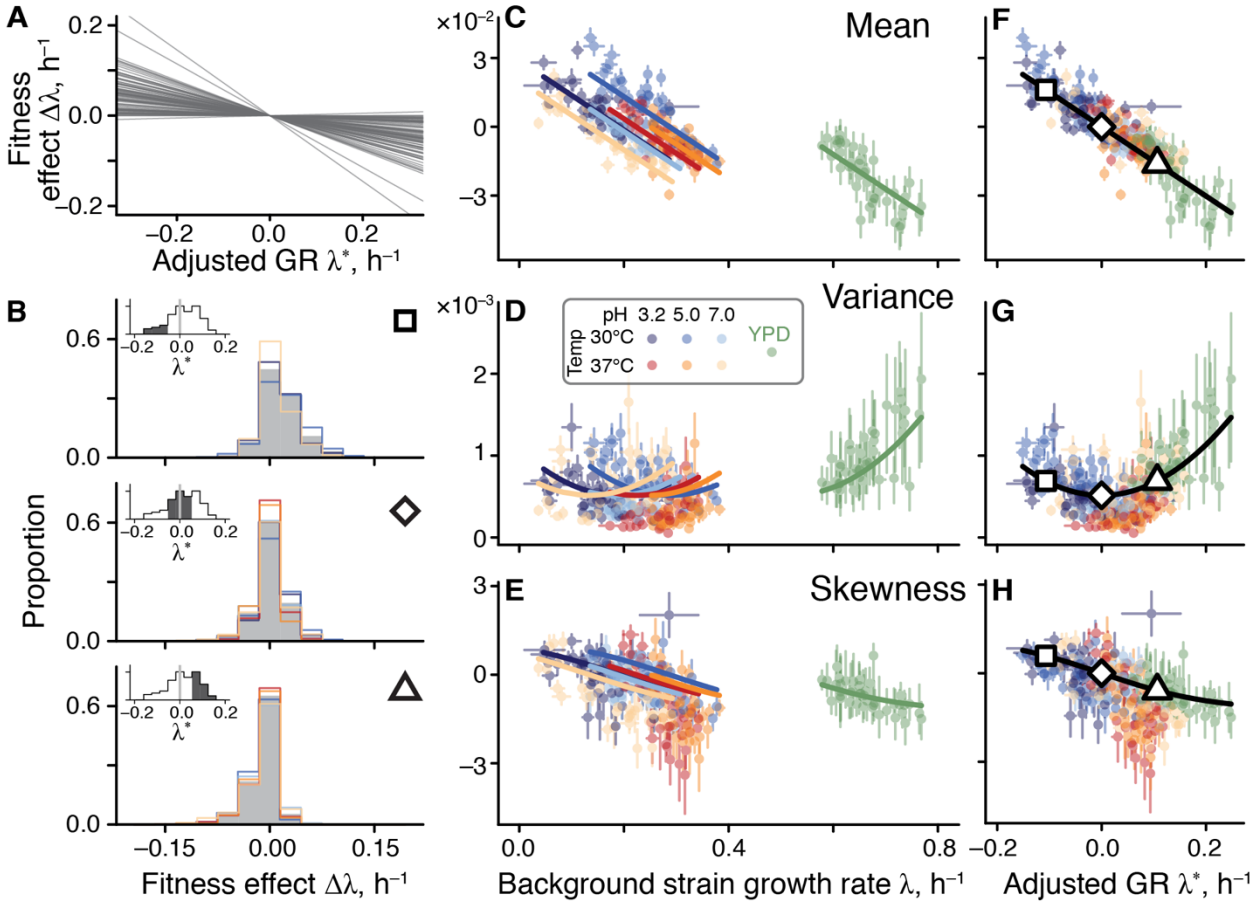

Figure 4. Generalized global epistasis equation explains the variation in the distribution of fitness effects across strains and environments. A. The effects of mutations in 30°C pH 7.0 according to the generalized global epistasis equation with the ζ-term set to zero. Each line represents a mutation. **B.** Estimated DFEs for strains whose adjusted GR is negative (top panel), approximately zero (middle panel) and positive (bottom panel). Gray bars show DFEs pooled across all environments, colored lines show DFEs for individual environments (colors are as in previous figures). Insets show the distributions of adjusted GRs for background strains, with the focal adjusted GR bin highlighted. Large square, rhombus and triangle are shown for reference with panels F,G,H. **C, D, E.** DFE moments plotted against the background strain GR. Error bars show ±1 standard errors (see Methods). Solid curves show the values calculated from Eq. (2) (Methods), and parameterized without the YPD data from Ref. (*42*). **F, G, H.** Same data as in C, D, E, but plotted against the adjusted GR. Theoretical curves explain 78%, 44%, and 33% of variation for the DFE mean, variance and skewness, respectively ($P < 2.2\times10^{-16}$).

To understand this prediction intuitively, consider an idealized case where the effects of all mutations vary according to the generalized global epistasis equation with ζ_{mge} set to zero (Figure 4A). Then, all mutations switch sign exactly at the pivot GR, so that a strain whose GR equals to $\bar{\lambda}_e$ has access only to neutral mutations. The DFE of such a strain has zero variance. Since the global epistasis lines for individual mutations spread out as the background GR deviates further from $\bar{\lambda}_e$ in either direction, the DFE variance increases. When $\zeta_{mge} \neq 0$, this overall pattern still holds but the variance at the pivot GR becomes positive (Figure S8).

Finally, the generalized global epistasis equation predicts that the skewness of the DFE ought to decline monotonically with λ_{ge} and cross zero again at the pivot GR. More generally, our model makes a qualitative prediction that the DFE varies across strains as a function of their environment-adjusted GR $\lambda^*_{ge} = \lambda_{ge} - \bar{\lambda}_e$ rather than as a function of their absolute GR λ_{ge}. Furthermore, in all environments, all odd central moments of the DFE are expected to be zero when the adjusted GR equals zero and all even central moments of the DFE are expected to achieve their minimum at the same value (Methods).

To test these predictions, we compared the empirical DFEs across environments. We find that pairs of strains with matched adjusted GRs have significantly more similar DFEs than pairs of strains with the same absolute GR in different environments or the same strain in different environments (Figure 4B and S9), consistent with our predictions. We then plotted the first three moments of the empirical DFEs against the unadjusted and adjusted GR in all environments. We find that these moments align remarkably well when plotted against the adjusted GR but not when plotted against the absolute GR (Figures 4C-H). As predicted, the DFE mean and skewness decline monotonically with the strain's adjusted growth rate and cross zero when the adjusted growth rate vanishes. As predicted, the DFE mean is a linear function whose slope is invariant across environments (Figure 4C,H). The most non-trivial prediction, that the DFE variance is a non-monotonic function of the adjusted GR whose minimum is achieved at zero adjusted GR, also holds.

The fact that all our predictions hold indicates that the linear generalized global epistasis equation with uncorrelated noise terms quantitatively captures the variation in the DFE shape across genotypes and environments. However, if the environment truly modulates only one effective parameter, the pivot GR, then we should be able to predict DFE shapes in any environment once its pivot GR is known. To test this prediction, we turned to our previous work where we measured DFEs of 163 yeast strains (a superset of the 42 strains used in this study) in a rich YPD environment (*42*). We estimated the pivot GR for this environment as the background GR where the mean of the DFE equals zero (see Methods for details). After GR adjustment, we found that our theoretical predictions quantitatively capture variation in the DFE moments across strains without any other fitted parameters (green points in Figure 4C-H).

These results show that microscopic global epistasis imposes simple, predictable, and general constraints on the G×G, G×E and G×G×E interactions at the macroscopic level. Specifically, the

external environment controls a single effective parameter, the pivot growth rate $\bar{\lambda}_e$; strains that grow much slower than $\bar{\lambda}_e$, have wide, positively skewed DFEs with a positive mean; strains whose GR is close to $\bar{\lambda}_e$ have narrow, symmetric DFEs with a zero mean; and strains that grow much faster than $\bar{\lambda}_e$ have wide, negatively skewed DFEs with a negative mean (Figure 4B).

To the extent that our observations hold beyond the specific set of strains, mutations and environments investigated in this study, they have a number of important implications. In genetics, the generalized global epistasis model can be incorporated into QTL analyses to improve predictions of the phenotypic effects of mutations. In evolutionary biology, our results point to the existence of a universal class of distributions of fitness effects of mutations, which could explain why evolutionary dynamics of fitness are so similar and predictable across systems (*30*, *39*, *46*, *53–55*). In conservation biology, the fact that low fitness genotypes have access to surprisingly large supplies of beneficial mutations gives hope that evolutionary rescue may prevent some species extinctions. More fundamentally, our results support the idea that epistasis effectively reduces the dimensionality of genotype-to-phenotype maps (*48*, *56*, *57*). These biological constraints that cause this remarkable dimensionality reduction are not well understood. Why they emerge and when they break down are exciting open questions in systems biology.

Acknowledgements:

We thank the members of the Kryazhimskiy and Meyer labs as well as Michael Desai, Terry Hwa and Erik Hom for insightful discussions. Computational work was assisted by the UC San Diego Triton Computing Cluster.

Funding:

This work was supported by an NIH T32 program (5T32GM133351-02, to S.M.A), the Curci Foundation (to S.M.A), the Christopher Wills endowed fellowship (to A.M), an NSF Postdoctoral Research Fellowships in Biology Program (Grant No. 2109800, to M.S.J.), an NSF Graduate Research Fellowship (to M.S.J.), The Burroughs Wellcome Fund (Career Award at Scientific Interface (1010719.01, to S.K.), The Alfred P. Sloan Foundation (FG-2017-9227, to S.K.), The Hellman Foundation (Hellman Fellowship, to S.K.), The National Institutes of Health (Grant No. 1R01GM137112, to S.K.).

Author contributions:

Conceptualization: SMA,SK; experimental design: AM, MSJ, SK; experiments: AM; analysis: SMA, SK; writing: SMA, MSJ, SK.

Competing interests:

None declared.

Data and materials availability:

Data described in the paper are presented in the supplementary materials. Raw sequencing data are publicly available at the NCBI Sequence Read Archive (accession no. PRJNA1028648), and all analysis code is available on GitHub (https://github.com/ardellsarah/Yeast_mutation_effects_across_strains_and_environments).

List of Supplementary Materials:

References and Notes

1. B. F. Koel, D. F. Burke, T. M. Bestebroer, S. van der Vliet, G. C. M. Zondag, G. Vervaet, E. Skepner, N. S. Lewis, M. I. J. Spronken, C. A. Russell, M. Y. Eropkin, A. C. Hurt, I. G. Barr, J. C. de Jong, G. F. Rimmelzwaan, A. D. M. E. Osterhaus, R. A. M. Fouchier, D. J. Smith, Substitutions near the receptor binding site determine major antigenic change during influenza virus evolution. *Science*. **342**, 976–979 (2013).

2. G. B. Dixon, S. W. Davies, G. A. Aglyamova, E. Meyer, L. K. Bay, M. V. Matz, Genomic determinants of coral heat tolerance across latitudes. *Science*. **348**, 1460–1462 (2015).

3. P. Promdonkoy, W. Mhuantong, V. Champreda, S. Tanapongpipat, W. Runguphan, Improvement in D-xylose utilization and isobutanol production in *S. cerevisiae* by adaptive laboratory evolution and rational engineering. *J. Ind. Microbiol. Biotechnol.* **47**, 497–510 (2020).

4. J. A. Plante, Y. Liu, J. Liu, H. Xia, B. A. Johnson, K. G. Lokugamage, X. Zhang, A. E. Muruato, J. Zou, C. R. Fontes-Garfias, D. Mirchandani, D. Scharton, J. P. Bilello, Z. Ku, Z. An, B. Kalveram, A. N. Freiberg, V. D. Menachery, X. Xie, K. S. Plante, S. C. Weaver, P.-Y. Shi, Spike mutation D614G alters SARS-CoV-2 fitness. *Nature*. **592**, 116–121 (2021).

5. J. M. Kreiner, S. M. Latorre, H. A. Burbano, J. R. Stinchcombe, S. P. Otto, D. Weigel, S. I. Wright, Rapid weed adaptation and range expansion in response to agriculture over the past two centuries. *Science*. **378**, 1079–1085 (2022).

6. B. Papp, R. A. Notebaart, C. Pál, Systems-biology approaches for predicting genomic evolution. *Nat. Rev. Genet.* **12**, 591–602 (2011).

7. P. L. Munday, R. R. Warner, K. Monro, J. M. Pandolfi, D. J. Marshall, Predicting evolutionary responses to climate change in the sea. *Ecol. Lett.* **16**, 1488–1500 (2013).

8. M. S. Johnson, G. Reddy, M. M. Desai, Epistasis and evolution: recent advances and an outlook for prediction. *BMC Biol.* **21**, 120 (2023).

9. H. A. Lindsey, J. Gallie, S. Taylor, B. Kerr, Evolutionary rescue from extinction is contingent on a lower rate of environmental change. *Nature*. **494**, 463–467 (2013).

10. Z. D. Blount, R. E. Lenski, J. B. Losos, Contingency and determinism in evolution: Replaying life's tape. *Science*. **362** (2018), doi:10.1126/science.aam5979.

11. T. N. Starr, J. M. Flynn, P. Mishra, D. N. A. Bolon, J. W. Thornton, Pervasive contingency and entrenchment in a billion years of Hsp90 evolution. *Proc. Natl. Acad. Sci. U. S. A.* **115**, 4453–4458 (2018).

12. D. M. Weinreich, N. F. Delaney, M. A. Depristo, D. L. Hartl, Darwinian evolution can follow only very few mutational paths to fitter proteins. *Science*. **312**, 111–114 (2006).

13. A. I. Khan, D. M. Dinh, D. Schneider, R. E. Lenski, T. F. Cooper, Negative epistasis between beneficial mutations in an evolving bacterial population. *Science*. **332**, 1193–1196 (2011).

14. H.-H. Chou, H.-C. Chiu, N. F. Delaney, D. Segrè, C. J. Marx, Diminishing returns epistasis among beneficial mutations decelerates adaptation. *Science*. **332**, 1190–1192 (2011).

15. L. I. Gong, M. A. Suchard, J. D. Bloom, Stability-mediated epistasis constrains the evolution of an influenza protein. *Elife*. **2**, e00631 (2013).

16. A. C. Palmer, E. Toprak, M. Baym, S. Kim, A. Veres, S. Bershtein, R. Kishony, Delayed commitment to evolutionary fate in antibiotic resistance fitness landscapes. *Nat. Commun.* **6**, 7385 (2015).

17. M. N. Mullis, T. Matsui, R. Schell, R. Foree, I. M. Ehrenreich, The complex underpinnings of genetic background effects. *Nat. Commun.* **9**, 3548 (2018).

18. J. M. Flynn, A. Rossouw, P. Cote-Hammarlof, I. Fragata, D. Mavor, C. Hollins 3rd, C. Bank, D. N. Bolon, Comprehensive fitness maps of Hsp90 show widespread environmental dependence. *Elife*. **9** (2020), doi:10.7554/eLife.53810.

19. C. W. Bakerlee, A. N. N. Ba, Y. Shulgina, J. I. R. Echenique, M. M. Desai, Idiosyncratic epistasis leads to global fitness-correlated trends. *Science*. **376**, 630–635 (2022).

20. A. Gupta, L. Zaman, H. M. Strobel, J. Gallie, A. R. Burmeister, B. Kerr, E. S. Tamar, R. Kishony, J. R. Meyer, Host-parasite coevolution promotes innovation through deformations in fitness landscapes. *Elife*. **11** (2022), doi:10.7554/eLife.76162.

21. R. M. L. Ang, S.-A. A. Chen, A. F. Kern, Y. Xie, H. B. Fraser, Widespread epistasis among beneficial genetic variants revealed by high-throughput genome editing. *Cell Genom*. **3**, 100260 (2023).

22. B. H. Good, M. M. Desai, The impact of macroscopic epistasis on long-term evolutionary dynamics. *Genetics*. **199**, 177–190 (2015).

23. J. L. Payne, A. Wagner, The causes of evolvability and their evolution. *Nat. Rev. Genet.* **20**, 24–38 (2018).

24. C. Bank, Epistasis and Adaptation on Fitness Landscapes. *Annu. Rev. Ecol. Evol. Syst.* **53**, 457–479 (2022).

25. C. Bank, S. Matuszewski, R. T. Hietpas, J. D. Jensen, On the (un)predictability of a large intragenic fitness landscape. *Proceedings of the National Academy of Sciences*. **113**, 14085–14090 (2016).

26. T. N. Starr, L. K. Picton, J. W. Thornton, Alternative evolutionary histories in the sequence space of an ancient protein. *Nature*. **549**, 409–413 (2017).

27. M. Lässig, V. Mustonen, A. M. Walczak, Predicting evolution. *Nature Ecology & Evolution*. **1**, 77 (2017).

28. D. A. Roff, A centennial celebration for quantitative genetics. *Evolution*. **61**, 1017–1032 (2007).

29. S. Kryazhimskiy, G. Tkacik, J. B. Plotkin, The dynamics of adaptation on correlated fitness landscapes. *Proc. Natl. Acad. Sci. U. S. A.* **106**, 18638–18643 (2009).

30. M. J. Wiser, N. Ribeck, R. E. Lenski, Long-term dynamics of adaptation in asexual populations. *Science*. **342**, 1364–1367 (2013).

31. S. M. Ardell, S. Kryazhimskiy, The population genetics of collateral resistance and sensitivity. *Elife*. **10** (2021), doi:10.7554/eLife.73250.

32. R. Kassen, T. Bataillon, Distribution of fitness effects among beneficial mutations before selection in experimental populations of bacteria. *Nat. Genet.* **38**, 484–488 (2006).

33. P. Domingo-Calap, J. M. Cuevas, R. Sanjuán, The fitness effects of random mutations in single-stranded DNA and RNA bacteriophages. *PLoS Genet.* **5**, e1000742 (2009).

34. S. F. Levy, J. R. Blundell, S. Venkataram, D. A. Petrov, D. S. Fisher, G. Sherlock, Quantitative evolutionary dynamics using high-resolution lineage tracking. *Nature*. **519**, 181–186 (2015).

35. A. Couce, M. Magnan, R. E. Lenski, O. Tenaillon, Predictability shifts from local to global rules during bacterial adaptation. *bioRxiv* (2023), , doi:10.1101/2022.05.17.492360.

36. D. Aggeli, Y. Li, G. Sherlock, Changes in the distribution of fitness effects and adaptive mutational spectra following a single first step towards adaptation. *Nat. Commun.* **12**, 5193 (2021).

37. J. E. Barrick, M. R. Kauth, C. C. Strelioff, R. E. Lenski, *Escherichia coli* rpoB mutants have increased evolvability in proportion to their fitness defects. *Mol. Biol. Evol.* **27**, 1338–1347 (2010).

38. R. C. MacLean, G. G. Perron, A. Gardner, Diminishing returns from beneficial mutations and pervasive epistasis shape the fitness landscape for rifampicin resistance in Pseudomonas aeruginosa. *Genetics*. **186**, 1345–1354 (2010).

39. S. Kryazhimskiy, D. P. Rice, E. R. Jerison, M. M. Desai, Global epistasis makes adaptation predictable despite sequence-level stochasticity. *Science*. **344**, 1519–1522 (2014).

40. S. Schoustra, S. Hwang, J. Krug, J. A. G. M. de Visser, Diminishing-returns epistasis among random beneficial mutations in a multicellular fungus. *Proc. Biol. Sci.* **283** (2016), doi:10.1098/rspb.2016.1376.

41. A. Wünsche, D. M. Dinh, R. S. Satterwhite, C. D. Arenas, D. M. Stoebel, T. F. Cooper, Diminishing-returns epistasis decreases adaptability along an evolutionary trajectory. *Nat Ecol Evol*. **1**, 61 (2017).

42. M. S. Johnson, A. Martsul, S. Kryazhimskiy, M. M. Desai, Higher-fitness yeast genotypes are less robust to deleterious mutations. *Science*. **366**, 490–493 (2019).

43. X. Wei, J. Zhang, Patterns and Mechanisms of Diminishing Returns from Beneficial Mutations. *Mol. Biol. Evol.* **36**, 1008–1021 (2019).

44. M. Lukačišinová, B. Fernando, T. Bollenbach, Highly parallel lab evolution reveals that epistasis can curb the evolution of antibiotic resistance. *Nat. Commun.* **11**, 3105 (2020).

45. M. S. Johnson, M. M. Desai, Mutational robustness changes during long-term adaptation in laboratory budding yeast populations. *Elife*. **11** (2022), doi:10.7554/eLife.76491.

46. K. Persson, S. Stenberg, M. J. Tamás, J. Warringer, Adaptation of the yeast gene knockout collection is near-perfectly predicted by fitness and diminishing return epistasis. *G3* . **12** (2022), doi:10.1093/g3journal/jkac240.

47. J. Diaz-Colunga, A. Skwara, K. Gowda, R. Diaz-Uriarte, M. Tikhonov, D. Bajic, A. Sanchez, Global epistasis on fitness landscapes. *Philos. Trans. R. Soc. Lond. B Biol. Sci.* **378**, 20220053 (2023).

48. G. Reddy, M. M. Desai, Global epistasis emerges from a generic model of a complex trait. *Elife*. **10**

(2021), doi:10.7554/eLife.64740.

49. J. S. Bloom, I. M. Ehrenreich, W. T. Loo, T.-L. V. Lite, L. Kruglyak, Finding the sources of missing heritability in a yeast cross. *Nature*. **494**, 234–237 (2013).

50. N. P. Mira, M. C. Teixeira, I. Sá-Correia, Adaptive response and tolerance to weak acids in *Saccharomyces cerevisiae*: a genome-wide view. *OMICS*. **14**, 525–540 (2010).

51. J. Ariño, Integrative responses to high pH stress in *S. cerevisiae*. *OMICS*. **14**, 517–523 (2010).

52. K. A. Morano, C. M. Grant, W. S. Moye-Rowley, The response to heat shock and oxidative stress in *Saccharomyces cerevisiae*. *Genetics*. **190**, 1157–1195 (2012).

53. E. R. Jerison, S. Kryazhimskiy, J. K. Mitchell, J. S. Bloom, L. Kruglyak, M. M. Desai, Genetic variation in adaptability and pleiotropy in budding yeast. *Elife*. **6**, 16858 (2017).

54. J. I. Rojas Echenique, S. Kryazhimskiy, A. N. Nguyen Ba, M. M. Desai, Modular epistasis and the compensatory evolution of gene deletion mutants. *PLoS Genet.* **15**, e1007958 (2019).

55. R. La Rosa, E. Rossi, A. M. Feist, H. K. Johansen, S. Molin, Compensatory evolution of *Pseudomonas aeruginosa's* slow growth phenotype suggests mechanisms of adaptation in cystic fibrosis. *Nat. Commun.* **12**, 1–15 (2021).

56. D. M. Lyons, Z. Zou, H. Xu, J. Zhang, Idiosyncratic epistasis creates universals in mutational effects and evolutionary trajectories. *Nat Ecol Evol*. **4**, 1685–1693 (2020).

57. S. Kryazhimskiy, Emergence and propagation of epistasis in metabolic networks. *Elife*. **10**, e60200 (2021).

Supplementary Materials for

Environment-Independent Distribution of Mutational Effects Emerges from Microscopic Epistasis

Sarah Ardell, Alena Martsul, Milo S. Johnson, Sergey Kryazhimskiy*

*E-mail: skryazhi@ucsd.edu

This PDF file includes:

1 Materials and methods

1.1 Strains and media

1.1.1 Background strains

Our "background strains" of yeast *S. cerevisiae* are a subset of a larger library of segregants that were previously generated from a cross between the lab strain BY and the vineyard strain RM (*1*) and whose evolutionary properties have been previously characterized (*2*, *3*, *4*). Specifically, our set of 42 background strains (listed in Table S4-Tab 2) is a subset of the strains used in the "Small Library" RB-TnSeq experiment described in Ref. (*3*). All the necessary strain details can be found in Refs. (*1*, *3*). Most importantly, our background strains differ from each other at approximately 25,000 loci and span nearly the full growth rate range in YPD measured in Ref. (*3*) (see Section 1.3.5). These strains also vary widely in both DFE mean (2.5-fold range) and variance (1.5-fold range) in YPD.

1.1.2 RB-TnSeq libraries

Background strains individually transformed with these RB-TnSeq libraries were kindly provided by Michael Desai (Harvard University). The design and construction of the RB-TnSeq libraries is described in detail in Ref. (*3*). Briefly, each background strain was transformed twice with the same set of 100 redundently barcoded transposon-insertion mutations, resulting in two biological replicates for each mutation in each strain, such that, within each transformation, each barcode uniquely tags a particular mutation and background strain (43% of barcodes were used in both transformations). The list of mutations and their corresponding barcodes is provided in Table S4-Tab 4. On average, each mutation was represented by 11 and 37 barcodes in the first and second transformation, respectively (see Table S4-Tab 4). Five mutations (IDs: 91 (nearby COA6), 51 (nearby FIT2), 6 (nearby MET2), 99 (nearby TDA11), 102 (nearby YSP2); see Table S4-Tab 4) that target intergenic regions were used as a neutral reference, as in Ref. (*3*). These reference mutations were represented by on an average 19 and 77 in barcodes in the two transformations.

1.1.3 Media and environments

Unless otherwise noted, all experiments were performed in synthetic complete medium (SC, 2% dextrose (VWR, #90000-904), 0.67% YNB + nitrogen powder (Sunrise Science Products, #1501-500), 0.2% synthetic complete drop-out powder mixture (Sunrise Science Products,#1300-030)). We added ampicillin (Amp) and tetracycline (Tet) at concentrations given in Table S2 into the medium to prevent bacterial contamination. Our environmental conditions differed by two factors, temperature (30°C and 37°C) and pH (3.2, 5.0, and 7.0). pH was maintained with the citrate-phosphate buffer (*5*), which was prepared using 1 M stocks of citric acid (VWR, # 97061-858) and K_2HPO_4 (VWR, #97062-234) following the protocol described in Ref. (*6*). Autoclaved media were pH-adjusted by adding the necessary volumes of sterile citric acid and K_2HPO_4 solutions and measuring the pH of the buffered media. If the pH of the buffered media deviated from the desired level, we further adjusted it by adding small volumes of 4 M HCl (Sigma-Aldrich #84435). Media was used within two days.

1.2 Experimental procedures

1.2.1 RB-TnSeq experiment

To estimate the effects of tn-mutations on the absolute growth rate (GR) in 42 background strains in 6 environments, we pooled the tn-mutant libraries of our background strains into multiple pools (see below for details) and maintained these pools in continuous growth in 150 ml of media in 500 ml flasks over the period of 48 hours with dilutions down to 5×10^7 cells and sampling every 12 hours. We carried out two replicate competition assays, one per independently transformed library (see Section 1.1.2).

Pre-growth and pooling. Prior to pooling, mutagenized strain libraries were defrosted and pre-grown for 24 h in 96-deep-well plates with 1 ml of media in each of our environments. Based on preliminary GR estimates, we grouped the background-strain libraries by their GR into three groups for the competition assays at 30°C and into two groups for the competition assays at 37°C. Each background strain was represented only in one group per temperature, with the exception of LK5-G01, which was added to each group as cross-group control. Group identities of each background strain can be found in Table S4-Tab 2. Thus, we propagated 6 cultures (3 GR groups $\times$ 2 biological replicates) in each of the 30°C environments and 4 cultures (2 GR groups $\times$ 2 biological replicates) in each of the 37°C environments for a total of 30 cultures.

After pre-growth, we measured OD600 of each mutant culture and converted it into cell density using a previously obtained calibration curve. Based on these density estimates, we pooled mutant cultures at approximately equal abundances, with a slight over-representation of those background strains whose preliminary GR estimates were lower. We then measured the density of each mixed culture again and transferred 5×10^7 cells into the corresponding competition flask. The remaining mixed T_0 cultures were frozen using the protocol described below.

Growth and dilution. Competitions were carried out in 150 ml of media in 500 ml baffled flasks (Pyrex No. 4446-500) in a shaking incubator (Eppendorf New Brunswick I26, 2.5 cm orbit) set to 150 rpm and appropriate temperature. Every 12 h, we estimated the cell density of each culture using plate-reader-based OD600 measurements and a previously obtained calibration curve (Table S4-Tab 3). Then, 5×10^7 cells were transferred into the fresh media. When the transfer volume exceeded 1 ml, we adjusted the volume of fresh media to maintain the consistent culture volume of 150 ml. All cultures were propagated for four growth and dilution cycles (48 hours), yielding five samples per culture.

Sampling and storage. We pelleted the cells from 50 ml of each cultures remaining after the transfer and froze the cell pellets at -70°C for subsequent DNA extraction and barcode sequencing.

1.2.2 Sequencing library preparation

We used the YeaStar Genomic Kit Protocol I (Zymo Research, #D2002) to extract gDNA from $\sim$ 1 ml of pelleted yeast cultures. To generate Illumina-ready dual-indexed amplicon library, we

used a two-step PCR protocol, modified from Ref. (7) as follows. All primer sequences can be found in Table S3.

First PCR. We combined 100 ng of extracted gDNA, 25 µl of OneTaq DNA polymerase Master Mix (New England BioLabs, #M0482L), 0.5 µl of 10 µM oAM-R2P-100-R01 primer, 0.5 µl of 10 µM oAM-R1P-20X-F01 primer, 1 µl of 50 µM $MgCl_2$, and molecular biology grade water up to the total volume of 50 µl. We used the following PCR protocol:

1. 94°C for 30 sec.
2. 94°C for 30 sec.
3. 50.5°C for 30 sec.
4. 68°C for 70 sec.
5. Repeat Steps 2–4 for a total of three times
6. 68°C for 5 min.

We purified this PCR product with AMPure XP magnetic beads (Beckman, #A36881) (1:1 ratio).

Second PCR. We combined 15 µl of purified PCR I product, 25 µl of OneTaq DNA polymerase Master Mix, 1 µl of 50 µM MgCl2, 1 µl of 10 µM N7XX primer (Nextera), and 1 µl of 10 µM S5XX primer (Nextera), and 7 µl of molecular biology grade H2O. We used the following PCR protocol:

1. 94°C for 30 sec.
2. 94°C for 30 sec.
3. 62°C for 30 sec.
4. 68°C for 70 sec.
5. Repeat Steps 2–4 for a total of 24 times
6. 68°C for 5 min.

The final PCR product was purified as above, run on a gel, extracted and purified with QIAquick PCR purification kit (Qiagen, #28106).

Sequencing. We sequenced the libraries with paired-end 150 bp reads on one HiSeq4000 platform and two HiSeq X10 platforms (Illumina).

1.2.3 Validation of estimated fitness effect of mutations

We were surprised by the high fraction of beneficial mutations identified in our RB-TnSeq experiment and carried out additional experiments designed to validate our fitness-effect estimates. To this end, after preliminary analyses, we selected a set of seven mutations: nearby MET2, nearby MET4, in NOT3, in PPM1, in RSC30, nearby TDA11, in MPC2 (Mutation IDs: 6,10, 117, 66, 71, 99, and 127, Table S4-Tab 4). We generated new RB-TnSeq libraries for these mutations and reconstructed them in two background strains, LK2-D07 and LK6-A05. Two of the selected mutations (nearby MET2 and nearby TDA11, IDs: 6, 99) were used as a neutral reference in the RB-TnSeq experiment. The mutation nearby MET4 (ID: 10) was identified to be neutral in the vast majority (74%) of genetic backgrounds and environments in the main experiment, and in all instances re-tested in the validation experiment. The remaining mutations were identified as more often beneficial in 30°C environments than 37°C and more often deleterious or neutral at 37°C than in 30°C. However, after final analyses, mutation 117 (in NOT3) no longer passed filters in the two focal strains and was excluded from the analyses.

The barcoded libraries for individual mutations were generated using the protocol described in Ref. (*3*). In total, we created 14 barcoded plasmid libraries (two replicated libraries per mutation), such that each library contained a unique set of barcodes. We then transformed these libraries into two background strains, LK2-D07 and LK6-A05, again following protocols described in Ref. (*3*). Transformant colonies were scraped and, after 24 h of additional growth in selective media, cultures were pelleted and frozen in 20% glycerol at −70°C. To determine which barcodes were associated with each mutation in each background strain, we sequenced each of the 14 yeast mutant libraries at the barcode locus using the same protocols as in Section 1.2.1. Barcode-mutation associations are provided in Table S4-Tab 8.

After generating the libraries of individual mutations, we estimated their fitness effects in two environments, 30°C pH 5.0 and 37°C pH 7.0, in each genetic background separately. We pre-grew 56 cultures (2 background strains × 7 mutations × 2 replicate mutant libraries × 2 environments) in the buffered SC media containing Amp (to avoid bacterial contamination) and either Nat or Hyg (required for selecting for the transformants, see Tables S4-Tab 2 and S2, and Ref. (*3*)) and incubated them in the two focal environments (30°C pH 5.0 and 37°C pH 7.0) for 24 h in test tubes shaken at 220 rpm. After measuring the concentrations of the grown cultures as described above (see Section 1.2.1), we created one mixed culture per background strain, per mutant library and per environment (2 environments × 2 strains × two biological replicates, for a total of 8 mixed cultures) as follows. We added each of the two neutral reference mutation cultures (IDs: 6,99) at frequency 25% each and we added each of the "query" mutant cultures (IDs: 10, 117, 66, 71, and 127) at 10%, such that initial ratio of reference and query mutants in each culture as 1:1. After estimating cell counts in these mixed cultures using OD600 (see Section 1.2.1), we transferred 5×10^7 cells to start the competition assay. The assays, sampling and sequencing library preparation were performed following the same protocols as in Section 1.2.1. Fitness effects of mutations estimated in this experiment are provide in Table S4-Tab 9.

1.3 Data Analysis

1.3.1 Code

All analysis code is written in R 4.3.1 and is available at

https://github.com/ardellsarah/Yeast_mutation_effects_across_strains_and_environments.

Packages used are listed in the beginning of all scripts. Computationally intensive analyses were run on the Triton Supercomputing Cluster (TSCC).

1.3.2 Counting barcodes

Raw barcode counts. Barcode counts for the main RB-TnSeq experiment (Section 1.2.1) were obtained using the BarcodeCounter2 package (*8*) with a pre-determined barcode-mutation association data from Ref. (*3*).

To determine barcode counts in the validation experiment, we first used the barcode sequencing data for individual mutation libraries (see Section 1.2.3) to associate each barcode sequence with a particular mutation and background strain (Table S4-Tab 4). To do so, we used regular expressions to extract all unique barcode sequences and clustered them using the `seq_cluster` function in R's bioseq package. We then used BarcodeCounter2 with the resulting barcode-mutation associations to extract raw barcode counts for each sample file.

Filtering. Because it is critical to have accurate reference barcode counts for the inference of fitness effects of mutations, we discarded all time points that contained less than 500 reference mutation counts for any given strain, replicate and environment. This filtering removed 1.3% (41,404/3,060,514) of strain-environment-replicate-time point combinations. Then, we retained only those barcodes that were present at three or more time points (in any given condition and replicate) at 5 or more counts at each time point.

1.3.3 Estimating growth rates of background strains and fitness effects of mutations

The central piece of our procedure for estimating the GRs of background strains and the fitness effects of mutations is the detection of "outlier" barcodes, i.e., those that have abnormally high or low GRs relative to other barcodes tagging the same mutation. Such outliers arise likely due to the tn-mutants acquiring secondary mutations either during the barcoding step or during the RB-TnSeq experiment. The outlier detection procedure requires preliminary estimates of fitness effects of barcodes tagging each mutation, which in turn requires a robust set of reference barcodes. Thus, our procedure consists of the following steps.

1. Estimate the GRs of all barcodes.
2. Detect and exclude outlier barcodes for reference mutations.
3. Obtain preliminary estimates of fitness effects of mutations based on the robust set of reference barcodes.

4. Detect and exclude outlier barcodes for non-reference mutations.

5. Estimate the background growth rates and the fitness effects of mutations in each biological replicate.

6. Pool estimates across replicates.

We describe the outlier detection algorithm at the end of this section. Suffices to say that this algorithm takes as input (i) the set of all barcodes tagging a given mutation (in a given genetic background, biological replicate and environment), (ii) the cell count estimates over time of all these barcoded lineages and (iii) the preliminary estimates of the fitness effects of these lineages, and it outputs a robust "outlier-free" set of barcodes corresponding to the mutation.

Before we describe our estimation procedure, recall that, in a given biological replicate r, each barcode k uniquely specifies a particular tn-mutation m and the background strain g into which this mutation is introduced (see Section 1.1.2). We denote the set of all barcodes tagging mutation m in genetic background g in replicate r by $\tilde{S}_{mgr}$. We also denote the set of five reference mutations by $\mathcal{S}^{\text{ref}}$ (see Section 1.1.2 and Table S4-Tab 4) and we denote the set of "reference barcodes", i.e., all barcodes that tag these reference mutations in the genetic background g and replicate r, by $\tilde{S}^{\text{ref}}_{gr} = \bigcup_{m\in\mathcal{S}^{\text{ref}}} \tilde{S}_{mgr}$. Tilde denotes the fact that these sets potentially include outlier barcodes.

Estimation of barcode GRs across time intervals. We first calculate the frequency of each barcode k (reference or non-reference) in each replicate r at each time point t by dividing its read count by the total count of all barcodes present in the same flask at that time. To estimate the number of cells N_{kret} that carry barcode k in repliate r in environment e at the sampling time t, we multiply barcode frequency by the total number of cells present in the flask at that time point (Table S4-Tab 3). We estimate the GR λ_{kret} of the barcode lineage k as

$$\lambda_{kret} = \frac{1}{\Delta t} \ln \frac{N_{kret+1}}{N_{kret}},$$

where Δt is the time between transfers (typically 12 h, Table S4-Tab 3).

Detection and exclusion of outlier reference barcodes. We obtain a preliminary estimate of the effect of each reference barcode k in background g, environment e and replicate r as

$$\widetilde{\Delta\lambda}_{kre} = \frac{1}{M_{kre}} \sum_t \left(\lambda_{kret} - \tilde{\lambda}_{gret}\right), \quad k \in \tilde{S}^{\text{ref}}_{gr},$$

where $\tilde{\lambda}_{gret} = \text{Median}\left\{\lambda_{kret} : k \in \tilde{S}^{\text{ref}}_{gr}\right\}$ and M_{kre} is the number of time intervals where barcode k is observed in environment e in replicate r. We use these estimates to apply our outlier detection algorithm (see below) and generate a robust set of reference barcodes S^{ref}_{gre} for each background strain g in each environment e and biological replicate r.

Preliminary estimates of fitness effects of mutations. For any barcode k tagging a non-reference mutation m in genotype g, we calculate its fitness effect in environment e and replicate r as

$$\Delta\lambda_{kre} = \frac{1}{M_{kre}} \sum_t \Delta\lambda_{kret}, \quad \text{for any } k \in \tilde{S}_{mgr}, \tag{S1}$$

where M_{kre} is the number of time intervals when this barcode is observed in environment e in replicate r, and

$$\begin{aligned} \Delta\lambda_{kret} &= \lambda_{kret} - \lambda_{gret}, \quad \text{for any } k \in \tilde{S}_{mgr}, \\ \lambda_{gret} &= \text{Median}\left\{\lambda_{kret} : k \in S^{\text{ref}}_{gre}\right\} \end{aligned} \tag{S2}$$

are robust estimates of the fitness effect of barcode k and GR of the background strain g, respectively, both at time interval t in environment e and replicate r. We then obtain a preliminary estimate of the fitness effect of each mutation m in genetic background g in environment e and biological replicate r as

$$\widetilde{\Delta\lambda}_{mgre} = \text{Median}\left\{\Delta\lambda_{kre} : k \in \tilde{S}_{mgr}\right\}. \tag{S3}$$

Detection and exclusion of outlier barcodes for non-reference mutations. We use preliminary fitness effect estimates given by equation (S3) and apply our outlier detection algorithm (see below) to generate a clean set of barcodes S_{mgre} for each mutation m in each background strain g in each environment e and biological replicate r.

Estimation of background GRs and fitness effects of mutations in each biological replicate. We estimate the GR of each background strain g in each environment e and biological replicate r as

$$\lambda_{gre} = \frac{1}{M_{gre}} \sum_t \sum_{k \in S^{\text{ref}}_{gre}} \lambda_{kret}, \tag{S4}$$

where M_{gre} is the number of barcode-time interval combinations at which λ_{kret} are estimated.

We estimate the fitness effect of each mutation m in each genetic background g environment e and biological replicate r as

$$\Delta\lambda_{mgre} = \frac{1}{M_{mgre}} \sum_t \sum_{k \in S_{mgr}} \Delta\lambda_{kret}, \tag{S5}$$

where $\Delta\lambda_{kret}$ are given by equation (S2) and M_{mgre} is the number of barcode-time interval combinations at which λ_{kret} are estimated.

Pooling estimates across biological replicates. We estimate how the fitness effects of mutations obtained using equation (S5) correlate across replicates. Since the replicates are highly correlated (Figure S2A-B), we pool the data from both replicates to obtain our final

estimates of background GRs and their standard errors,

$$\lambda_{ge} = \frac{1}{M_{ge}} \sum_{r,t} \sum_{k \in S^{\text{ref}}_{gre}} \lambda_{kret}, \tag{S6}$$

$$\sigma^{\lambda}_{ge} = \left[\frac{1}{M_{ge}(M_{ge}-1)} \sum_{r,t} \sum_{k \in S^{\text{ref}}_{gre}} (\lambda_{kret} - \lambda_{ge})^2 \right]^{\frac{1}{2}}, \tag{S7}$$

where M_{ge} is the number of barcode-replicate-time combinations at which λ_{kret} are estimated for background g in environment e. We estimate the fitness effects of mutations and their standard errors

$$\Delta\lambda_{mge} = \frac{1}{N_{mge}} \sum_{r,t} \sum_{k \in S_{mgr}} \Delta\lambda_{kret}, \tag{S8}$$

$$\sigma^{\Delta\lambda}_{mge} = \left[\frac{1}{M_{mge}(M_{mge}-1)} \sum_{r,t} \sum_{k \in S_{mgre}} (\Delta\lambda_{kret} - \Delta\lambda_{mge})^2 \right]^{\frac{1}{2}}, \tag{S9}$$

where M_{mge} is the number of barcode-replicate-time combinations at which $\Delta\lambda_{kret}$ are estimated for mutation m in background strain g and environment e.

The distributions of standard errors for background GRs and fitness effects are shown in Figure S2. The average standard error of the background GR is

$$\sigma_{\text{bg}} = 1.9 \times 10^{-3}\ \text{h}^{-1} \tag{S10}$$

and the average standard error of fitness effect is

$$\sigma_{\text{mut}} = 6.3 \times 10^{-3}\ \text{h}^{-1}. \tag{S11}$$

The comparison of these values shows that the noise in non-reference barcodes is typically more than 3-fold higher than noise in reference barcodes. Therefore, we note that, although equation (S9) ignores noise in reference barcodes, incorporating this noise would likely introduce only a small correction.

Detection of outlier barcodes. The goal of this procedure is to detect those barcodes whose frequencies either rise or fall unexpectedly quickly compared to the other barcodes tagging the same mutation in the same genetic background. To this end, we follow the method developed in Ref. (*3*), which takes as input the set of all barcodes k tagging a given mutation (in a given genetic background, biological replicate and environment), the corresponding cell counts N_{kt} at each time sampling t and the preliminary estimates $\widetilde{\Delta\lambda}_k$ of the fitness effects of all these barcoded lineages. Briefly, we calculate the "within-mutation" frequencies f_{kt} at time t as $f_{kt} = N_{kt}/\left(\sum_{k'} N_{k't}\right)$. All barcoded lineages tagging the same mutation should grow at the same rate. Therefore, we expect all frequencies f_{kt} to be constant over time, barring demographic and sampling noise. To determine which frequency trajectories are inconsistent

with this neutral expectation, we create a "within-mutation-neutral reference" (WMNR) set of barcodes whose preliminary fitness effect $\widetilde{\Delta\lambda}_k$ is within 0.01 of the median fitness effect of all these barcodes. Then, we fit two models to all frequency trajectories f_{kt} for those barcodes that are not in the WMNR set. In the neutral model, each query barcode's trajectory does not systematically change relative to the pooled WMNR trajectory. In the model with selection, query barcode's frequency can systematically increase or decrease. We find the log-likelihood of the observed barcode trajectory given each of the two models and calculate the likelihood ratio (LR) statistic. We conservatively exclude all barcodes with the LR statistic values greater than 40, corresponding to a P-value from a χ^2 distribution with 1 d.f. $< 10^{-9}$. This algorithm returns a "clean" subset of barcodes that tag a given mutation (in a given genetic background, environment and replicate).

Using this method, we exclude a total of 2.4% (16,799/683,754) of barcode-replicate combinations.

1.3.4 Calling beneficial and deleterious mutations

To call each mutation as either beneficial, deleterious or neutral in each genetic background and environment, we construct the 99% confidence interval using a normal distribution with the mean equal to $\Delta\lambda_{mge}$ (equation (S8)) and variance equal to the standard error of the mean $\sigma^{\Delta\lambda}_{mge}$ (equation (S9)). Mutations whose entire confidence interval is below zero are called deleterious and those whose entire confidence interval is above zero are called beneficial. All other mutations, i.e., those whose confidence interval spans zero, are called neutral. We identify a total of 7286 non-neutral mutation-genotype-environment combinations out of 18551 tested. If all mutations were truly neutral, we would expect to call 1% or ~ 185 of them non-neutral by chance, yielding the false discovery rate of $185/7286 = 2.5\%$.

1.3.5 Growth rates of background strains in YPD

Johnson et al (2019) estimated the mean, variance and skewness of tn-insertion DFEs in 163 yeast background strains g in rich YPD medium, as well as the fitness s_g of these strains relative to a common reference strain (*3*). They also separately measured exponential GR λ_g for a subset of their background strains. Using this subset of strains, we find a very good linear relationship between λ_g and s_g in YPD ($P = 9.632 \times 10^{-9}$, $R^2 = 0.97$),

$$\lambda_g = 0.9729\, s_g + 0.6732. \tag{S12}$$

We use equation (S12) to estimate the GR in YPD for all 163 strains.

1.3.6 Variation of growth rates and mutational effects across environments

To assess how the GR rank order of background strains varies across environments, we first find the median GR of all strains in each environment. We then call a strain as "above median" if its GR is above this median by at least one unit of its standard error σ^{λ}_{ge} (equation (S7)). Analogously, we call a strain as "below median" if its GR is below the median by at least σ^{λ}_{ge}. Any strain that is identified at least once as above median GR and at least once as below median GR was labelled as "Rank change" in Figure S6).

We assessed rank-order changes of mutations across environments within each strain using an analogous procedure (Figure S7).

1.3.7 Models of global epistasis

We fit equations (1) and (2) using `lm` function in R. To estimate the "pivot GR", we regress a_{me} against b_{me} (both estimated from the fit of (1)) with zero intercept and estimate pivot GR $\bar{\lambda}_e$ as the slope of this linear relationship.

Accounting for measurement errors in the calculation of global epistasis slopes. As pointed out by Berger and Postma (*9*), negative slopes in equation (1) (for any given mutation m and environment e) can arise spuriously due to fact that measurements errors in λ_{ge} and $\Delta\lambda_{mge}$ are correlated. Using the same approach as in Ref. (*9*), we compute the corrected correlation coefficient between $\Delta\lambda_{mge}$ and λ_{ge} across background genotypes for a fixed mutation m in a fixed environment e as

$$\rho'\left(\Delta\lambda_{mge}, \lambda_{ge}\right) = \frac{\mathrm{Cov}\left(\Delta\lambda_{mge}, \lambda_{ge}\right) + \sigma^2_{\mathrm{bg}}}{\sqrt{\left(\mathrm{Var}\left(\lambda_{ge}\right) - \sigma^2_{\mathrm{bg}}\right)\,\left(\mathrm{Var}\left(\Delta\lambda_{mge}\right) - \sigma^2_{\mathrm{bg}} - \sigma^2_{\mathrm{mut}}\right)}}. \tag{S13}$$

Here λ_{mge} and $\Delta\lambda_{mge}$ are given by equations (S6) and (S8), respectively; σ^2_{bg} and σ^2_{mut} are the measurement noise variance for GR of the background and mutant strains, respectively, which can be calculated from expressions (S10) and (S11), respectively; and

$$\begin{aligned}
\langle X \rangle &= \frac{1}{K}\sum_g X_g, \\
\mathrm{Var}\left(X\right) &= \frac{1}{K-1}\sum_g (X_g - \langle X \rangle)^2, \\
\mathrm{Cov}\left(X, Y\right) &= \frac{1}{K-1}\sum_g (X_g - \langle X \rangle)(Y_g - \langle Y \rangle).
\end{aligned}$$

are the estimates of the mean, variance and covariance, taken over all background genotypes g. We find that the uncorrected correlation coefficient

$$\rho\left(\Delta\lambda_{mge}, \lambda_{ge}\right) = \frac{\mathrm{Cov}\left(\Delta\lambda_{mge}, \lambda_{ge}\right)}{\sqrt{\mathrm{Var}\left(\lambda_{ge}\right)\ \mathrm{Var}\left(\Delta\lambda_{mge}\right)}}$$

deviates very little from the corrected correlation coefficient ρ' given by equation (S13) (see Figure S2D), indicating that the global epistasis trends we observe are not spurious.

Comparing distribution of slopes and intercepts across environments. We tested how the distributions of fitted slopes and intercepts vary across environments using three different pairwise tests (Figure S4).

1. A Kolmogorov–Smirnov test assess the overall differences between two distributions.

2. A paired t-test assess the differences between the means of the two distributions.

3. An F-test assess the difference between the variances of the two distributions.

All tests were performed using the stats package in R, and the raw P-values were adjusted using the Benjamini-Hochberg multiple testing correction. Adjusted P-values are reported in Figure S4A.

Comparing variable slopes and invariant slopes models for individual mutations. In addition to the full "variable slopes" model (equation (1)) in which a mutation can have different slopes in different environments, we also fit an "invariant slopes" model to our data in which every mutation has a single environment-invariant slope. We compared that variable and invariant slopes models using the likelihood ratio test and found that, for the majority of mutations, we could not reject the invariant slopes model in favor of the variable slopes model which has 5 more parameters (Figure S4C). We then calculated the adjusted R^2_{adj} for both the invariant and variable slopes models for each mutation using the R function `lm`,

$$R^2_{\text{adj}} = 1 - \left((1 - R^2) \frac{n-1}{n-k-1} \right),$$

where R^2 is the standard coefficient of determination, n is the number of observations and k is the number of predictors. In this case, n is the number of unique genotype-environment combinations in which the mutation is measured, and k is twice the number of environments in which the mutation is measured (variable slopes model) or the number of such environments plus one (invariant slopes model). This adjustment helps identify potential over-fitting by penalizing a high number of parameters relative to the number of observations.

Analysis of microscopic epistasis slopes. To determine whether global-epistasis slopes for a given mutation are statistically distinguishable across environments, we estimate these slopes as described above using the `lm` function in R. Along with the maximum likelihood estimates of the slopes, this function returns the standard errors of these estimates. Then, for each pairwise slope comparison, we calculate the difference between the slopes and estimate the associated error variance as the square root of the summed squared errors. Assuming that errors are normally distributed, we calculate the P-value for the observed error. We then apply the Benjamini-Hochberg multiple testing correction for all pairwise comparisons for a given mutation and obtain adjusted P-values. A pair of slopes is then called significantly different if the adjusted P-value is below 0.05.

1.3.8 Variance partitioning for the sign of mutations

Let Y_{mge} be the observed sign of mutation m in genetic background g in environment e, such that $Y_{mge} = \pm 1$. The total variance in the observed signs of mutations is

$$V^{\text{tot}} = \frac{1}{K-1} \sum_{m,g,e} \left(Y_{mge} - \overline{Y} \right)^2,$$

where

$$\overline{Y} = \frac{1}{K} \sum_{m,g,e} Y_{mge}$$

is the average sign of the mutational effect and $K = \sum_{m,g,e} 1$ is the total number of mutations measured across all genotypes and environments.

Let the true fitness effect of mutation m in genetic background g in environment e (without measurement noise) be

$$s_{mge} = G_{mge} + \xi_{mge},$$

where $G_{mge} = a_{me} + b_{me}\,\lambda_{ge}$ is the global epistasis term, λ_{ge} is the GR of background strain g in environment e, and ξ_{mge} is the idiosyncractic epistasis term (see equation (1)). Then, the probability that the observed sign of this mutation is positive is

$$p_{mge}^{\mathrm{gl+id}} = \Pr\left(Y_{mge} = 1\right) = \frac{1}{\sqrt{2\pi\sigma_{mge}^2}} \int_0^\infty \exp\left[-\frac{(x - s_{mge})^2}{2\sigma_{mge}^2}\right] dx, \tag{S14}$$

where σ_{mge}^2 is the variance of the measurements noise for mutation m in background g in environment e. The super-index $\mathrm{gl} + \mathrm{id}$ indicates that this probability takes into account both global and idiosyncratic epistasis. We estimate $p_{mge}^{\mathrm{gl+id}}$ using equation (S14) with s_{mge} and σ_{mge} given by equations (S8) and (S9). This allows us to calculate the expected sign of mutation m in background g in environment e,

$$\overline{Y}_{mge}^{\mathrm{gl+id}} = 2\,p_{mge}^{\mathrm{gl+id}} - 1$$

and estimate the variance in the mutational sign attributed solely to measurement noise,

$$V^{\mathrm{n}} = \frac{1}{K-1} \sum_{m,g,e} \left(Y_{mge} - \overline{Y}_{mge}^{\mathrm{gl+id}}\right)^2. \tag{S15}$$

In a model without idiosyncratic epistasis, the probability p_{mge}^{gl} that the observed sign of the mutational effect is positive can be estimated using the same equation (S14), but with

$$\begin{aligned} s_{mge} &= G_{mge}, \\ \sigma_{mge}^2 &= \frac{1}{M_{me}(M_{me}-1)} \sum_{r,t,g'} \sum_{k \in S_{mg're}} \left(\Delta\lambda_{kret} - G_{mg'e}\right)^2, \end{aligned}$$

where $\Delta\lambda_{kret}$ are estimated with equation (S2) and M_{me} is the number of barcode-genotype-replicate-time combinations at which $\Delta\lambda_{kret}$ are estimated for mutation m and environment e.

Thus, the variance in the mutational signs attributed to both idiosyncratic epistasis and measurement noise is

$$V^{\mathrm{id+n}} = \frac{1}{K-1} \sum_{m,g,e} \left(Y_{mge} - \overline{Y}_{mge}^{\mathrm{gl}}\right)^2,$$

where

$$\overline{Y}_{mge}^{\mathrm{gl}} = 2\,p_{mge}^{\mathrm{gl}} - 1$$

is the expected sign of mutation m in background g in environment e in the model without idiosyncratic epistasis. Thus, we can partition the total variance V^{t} into the global, idiosyncratic and noise components as follows. Variance V^{n} given by equation (S15) is attributed to noise, variance

$$V^{\mathrm{id}} = V^{\mathrm{id+n}} - V^{\mathrm{n}}$$

is attributed to idiosyncratic epistasis, and variance

$$V^{\mathrm{gl}} = V^{\mathrm{tot}} - V^{\mathrm{id+n}}$$

is attributed to global epistasis.

1.3.9 Empirical DFEs

For YPD, we use the estimates of DFE moments and their corresponding standard errors obtained in Ref. (*3*). In each other environment e and for each background strain g, we use the fitness effect estimates $\Delta\lambda_{mge}$ obtained from equation (S8) to estimate the mean $\langle\Delta\lambda\rangle_{ge}$, variance $\mathrm{Var}_{ge}[\Delta\lambda]$ and skewness $\mathrm{Skew}_{ge}[\Delta\lambda]$ of the empirical DFEs as

$$\begin{aligned}
\langle\Delta\lambda\rangle_{ge} &= \frac{1}{K_{ge}}\sum_m \Delta\lambda_{mge}, \\
\mathrm{Var}_{ge}[\Delta\lambda] &= \frac{1}{K_{ge}-1}\sum_m \left(\Delta\lambda_{mge} - \langle\Delta\lambda\rangle_{ge}\right)^2, \\
\mathrm{Skew}_{ge}[\Delta\lambda] &= \frac{\frac{1}{K_{ge}}\sum_m \left(\Delta\lambda_{mge} - \langle\Delta\lambda\rangle_{ge}\right)^3}{\left(\mathrm{Var}_{ge}[\Delta\lambda]\right)^{\frac{3}{2}}}.
\end{aligned}$$

Here, K_{ge} is the number of mutations whose effects were estimated in background strain g in environment e. To estimate the uncertainty in these estimates, we resampled 70 random mutations from each empirical DFE with replacement (bootstrapping). For each resampled mutation, we drew its fitness effect from a normal distribution with mean $\Delta\lambda_{mge}$ (given by equation S8) and standard deviation $\sigma^{\Delta\lambda}_{mge}$ (given by equation S9). We performed 300 iterations of this procedure.

Sensitivity of DFE moment estimates to missing measurements. In pooled cultures, slow growing mutants may go extinct during the competition assay, which could prevent us from estimating their effects and lead to biases in our estimates of the DFE moments. In particular, highly deleterious mutations missing from the data could leads us to overestimate the DFE mean, underestimate the DFE variance and overestimate DFE skewness. Furthermore, we expect that these biases would be stronger in slower growing background strains, which could produce spurious declines in DFE mean and skewness with the background-strain GR.

As described above, we sought to mitigate this potential issue experimentally by competing our mutants in groups with similar GRs (see Section 1.2.3). However, these spurious effects may still be present in our data. To investigate how severe these effects might be, we plotted the number of mutations for which we have reliable fitness-effect estimates against the respective

background strain GR. We found that the number of mutations per strain varies little with the background-strain GR in 30°C environments (Figure S10B), but it does vary in the expected direction in 37°C environments. However, since this analysis does reveal the fitness effects of missing mutations, this observation alone does not imply that our estimates of DFE moments are biased for slow-growing strains in 37°C environments. Thus, we carried out two additional analyses to further probe probe the extent of these potential biases.

First, we eliminated all strains from our analysis for which we measured less than 60 mutations (bottom 24%) and replotted DFE moments for this reduced number of strains (Figure S10A) and found that all the trends found in the full data set remain in this reduced data set (compare Figure S10C and 4). Second, in each environment, we identified the set of 40 mutations all of which were measured in the maximum number of strains in that environment, which ranged from 16 to 40 strains, depending on environment. We then restricted our analysis of DFE moments to these strains and mutations, thereby creating a reduced data set without any missing measurements. We found that the DFE moments recapitulate the trends reported for the full data set (compare Figures S10D and 4). Based on these analyses, we conclude that the trends in the DFE moments that we report are not spurious results of missing measurements.

Variation of the DFEs with adjusted GR. We carried a series of pairwise DFE comparisons across strains and/or environments. To this end, we created matched pairs of background strains using three methods:

1. *Adjusted GR matching.* We matched each background strain g_1 in environment e_1 with another background strain $g_2 \neq g_1$ in a different environment $e_2 \neq e_1$, such that the adjusted GR $\lambda^*_{g_2e_2}$ of the latter strain was most similar to the former strain among all other strain-environment combinations.

2. *Raw GR matching.* We carried out the same procedure as above except we matched raw GRs.

3. *Strain matching.* We matched each background strain g_1 in environment e_1 with itself in another environment e_2 such that $\lambda_{g_1e_2}$ was the closes to $\lambda_{g_1e_1}$.

Then, we compared the DFEs of the two matched strain-environment combinations using four metrics of similarity shown in Figure S9.

1.3.10 QTL analysis

With only 42 background strains, we have little power to identify QTLs *de novo*. Instead, we assess whether certain loci identified in previous studies (*2*, *3*) help explain some of the idiosyncratic epistasis. Specifically, four loci Chr XIV-376315 (KRE33), ChrXII-646707, ChrXIV-470303, and ChrXV-154799 were identified as having significant explanatory power on the fitness effect of multiple mutations by both Jerison et al (2017) (Ref. (*2*)) and Johnson et al (2019) (Ref. (*3*)), and we tested whether these candidate loci also have significant explanatory power in our data. We used ANOVA to determine whether the addition of these four loci to the generalized global epistasis model (equation (2)) significantly reduced the proportion of unexplained variance for

each mutation. If the contribution of a locus was significant at P-value 0.05, then we also calculated the fraction of variance explained by this locus above and beyond the generalized global epistasis model.

Out of a total of 89 mutations in which our models explained some variance in their fitness effects, we found two mutations (in genes UBP3 (ID 95) and STH1 (ID 41)) where 38% and 21% of overall variance was jointly explained by the four candidate QTLs, corresponding to 59% and 27% of the explained variance in each mutation, respectively. In one additional mutation, nearby HO (ID 78), these candidate loci together explain 8% of the overall variance in its effect, but this comprises 100% of the explained variance. For the remaining 97% (86/89) mutations, the four candidate loci together explain less than 14% of overall variance, with a median of only 3% (interquartile interval [1.8%, 5.7%]), corresponding to a median of 6.8% of the total explained variance within each mutation (interquartile interval [3.9%, 15.6%], Supplementary Table S4-Tab 10).

1.4 Theoretical calculation of DFE moments

Here we derive the moments of the distribution of fitness effects (DFE) of mutations from the generalized global epistasis equation (equation (2) in the main text). Since we consider the environment fixed, we drop the subindex e. To simplify notations, we will denote the adjusted GR of the background strain g by $F_g \equiv \lambda_g^*$ and we denote the fitness effect of a mutation in this background by $s_g \equiv \Delta\lambda_g$. To derive DFE moments, we assume that the effects of mutations s are drawn from a continuous distribution defined by equation

$$s_g = b\, F_g + \eta + \xi_g, \tag{S16}$$

which is the continuous analog of equation (2). Here b and η are the slope and the y-intercept of the focal mutation, and ξ_g is the idiosyncratic epistasis of this mutation in the background strain g. We assume that b and η are independent, and that b has probability density $p_{\rm sl}$, η is normally distributed with zero mean and variance $\sigma^2_{\rm pivot}$. We also assume that ξ_g is normally distributed with zero mean and variance $\sigma^2_{\rm id}$ (which can in principle depend on b, see Ref. (*10*)). Thus, conditional on b and η, the fitness effects s_g of the mutation in the background g is a normal random variable with distribution with mean $\langle s|b,\eta\rangle = b\, F_g + \eta$ and variance $\sigma^2_{\rm id}$. Then, the DFE $p_g(s)$ in the background g with adjusted GR F_g is given by

$$p_g(s) = \int_{-\infty}^{\infty} db\, p_{\rm sl}(b) \int_{-\infty}^{\infty} d\eta\, N\left(\eta; 0, \sigma^2_{\rm pivot}\right)\, N\left(s; b\, F_g + \eta, \sigma^2_{\rm id}\right), \tag{S17}$$

where $N(x;\mu,\sigma^2)$ is the normal probability density with mean m and variance σ^2. Since

$$N\left(s; b\, F_g + \eta, \sigma^2_{\rm id}\right) = N\left(\eta; s - b\, F_g, \sigma^2_{\rm id}\right)$$

and since

$$N\left(x;\mu_1,\sigma_1^2\right)\, N\left(x;\mu_2,\sigma_2^2\right) = \frac{1}{\sqrt{2\pi\left(\sigma_1^2+\sigma_2^2\right)}} \exp\left(-\frac{(\mu_1-\mu_2)^2}{2\left(\sigma_1^2+\sigma_2^2\right)}\right)\, N(x,\mu_3,\sigma_3^2),$$

where $\mu_3 = \frac{\sigma_1^{-2}}{\sigma_1^{-2}+\sigma_2^{-2}}\,\mu_1 + \frac{\sigma_2^{-2}}{\sigma_1^{-2}+\sigma_2^{-2}}\,\mu_2$ and $\sigma_3^2 = \frac{1}{\sigma_1^{-2}+\sigma_2^{-2}}$ for any μ_1, μ_2, σ_1^2 and σ_2^2, the integral with respect to η can be taken, such that the expression (S17) simplifies to

$$p_g(s) = \int_{-\infty}^{\infty} db\, p_{\rm sl}(b)\, N\left(s; b\,F_g, \tilde{\sigma}^2\right), \tag{S18}$$

where we denoted $\tilde{\sigma}^2 = \sigma_{\rm pivot}^2 + \sigma_{\rm id}^2$.

Equation (S18) allows us to compute the DFE mean as

$$\langle s\rangle = \int_{-\infty}^{\infty} db\, p_{\rm sl}(b) \int_{-\infty}^{\infty} ds\, s\, N\left(s; b\,F_g, \tilde{\sigma}^2\right) = \langle b\rangle\, F_g \tag{S19}$$

and higher central moments of the DFE as

$$M^{(n)}[s] = \int_{-\infty}^{\infty} db\, p_{\rm sl}(b) \int_{-\infty}^{\infty} ds\, \left(s - \langle b\rangle\, F_g\right)^n\, N\left(s; b\,F_g, \tilde{\sigma}^2\right) \tag{S20}$$

Using expression (S20) and the fact that

$$s - \langle b\rangle\, F_g = (s - bF_g) + (b - \langle b\rangle)\, F_g$$

we obtain the following explicit expressions for the DFE variance $\mathrm{Var}[s]$ and its third central moment $M^{(3)}[s]$,

$$\begin{aligned}
\mathrm{Var}[s] \;\equiv\; M^{(2)}[s] &= \int_{-\infty}^{\infty} db\, p_{\rm sl}(b) \left[\tilde{\sigma}^2 + (b - \langle b\rangle)^2\, F_g^2\right] \\
&= \mathrm{Var}[b]\; F_g^2 + \sigma_{\rm pivot}^2 + \int_{-\infty}^{\infty} p_{\rm sl}(b)\, \sigma_{\rm id}^2\, db, \qquad \text{(S21)} \\
M^{(3)}[s] &= \int_{-\infty}^{\infty} db\, p_{\rm sl}(b) \left[3\tilde{\sigma}^2\, (b - \langle b\rangle)\, F_g + (b - \langle b\rangle)^3\, F_g^3\right] \\
&= M^{(3)}[b]\; F_g^3 + 3F_g \int_{-\infty}^{\infty} p_{\rm sl}(b)\, \sigma_{\rm id}^2\; (b - \langle b\rangle)\; db. \qquad \text{(S22)}
\end{aligned}$$

Here $\mathrm{Var}[b]$ and $M^{(3)}[b]$ are the variance and the third central moment of the distribution $p_{\rm sl}(b)$ of global epistasis slopes, respectively.

We find that the variance of residuals and slopes are correlated (Figure S4C). Thus, we set $\sigma_{\rm id}^2 = -\alpha\, b$, and the expressions (S21) and (S22) become

$$\begin{aligned}
\mathrm{Var}[s] &= -\alpha\; \langle b\rangle + \sigma_{\rm pivot}^2 + \mathrm{Var}[b]\; F_g^2, \qquad \text{(S23)} \\
M_g^{(3)}[s] &= -3\alpha\, \mathrm{Var}[b]\; F_g + M^{(3)}[b]\; F_g^3. \qquad \text{(S24)}
\end{aligned}$$

and the skewness of the DFE is given by

$$\mathrm{Skew}_g[s] = \frac{M_g^{(3)}[s]}{\left(\mathrm{Var}_g[s]\right)^{3/2}} = \frac{-3\alpha\, F_g / \sqrt{\mathrm{Var}[b]} + \mathrm{Skew}[b]\; F_g^3}{\left(\frac{-\alpha\,\langle b\rangle + \sigma_{\rm pivot}^2}{\mathrm{Var}[b]} + F_g^2\right)^{3/2}}. \tag{S25}$$

Equations (S19), (S23) and (S25) show that when $F_g = 0$, DFE mean and skewness are zero and the DFE variance achieves its minimal value $\sigma_{\rm id}^2$. Furthermore, since Skew $[b] < 0$, DFE skewness monotonically declines from $-\text{Skew}\,[b] > 0$ to Skew $[b] < 0$.

To show that all odd moments of the DFE vanish when $F_g = 0$, we notice that, when $F_g = 0$, equation (S18) simplifies to

$$p_g(s) = N\left(s; 0, \tilde{\sigma}^2\right), \tag{S26}$$

i.e., the DFE is a normal distribution, which implies that all its odd central moments vanish. To show that all even moments of the DFE reach their minimum at $F_g = 0$, we differentiate expression (S20) with respect to F_g at $F_g = 0$ and obtain

$$\left.\frac{dM^{(n)}\left[s\right]}{dF}\right|_{F_g=0} = \int_{-\infty}^{\infty} db\, p_{\rm sl}(b) \left[-n\left\langle b\right\rangle M^{(n-1)}\left[s|b\right] + \frac{b}{\tilde{\sigma}^2} M^{(n+1)}\left[s|b\right]\right].$$

where $M^{(n)}\left[s|b\right] = \int_{-\infty}^{\infty} s^n N\left(s; 0, \tilde{\sigma}^2\right) ds$ is the nth central moment of a normal distribution with mean zero and variance $\tilde{\sigma}^2$. Therefore, when n is even, $\left.\frac{dM^{(n)}[s]}{dF}\right|_{F_g=0}$ vanishes because all odd central moments of a normal distribution are zero. To see that $M^{(n)}\left[s\right]$ achieve their minimum at $F_g = 0$ for any even n, we find that the second derivative of $M^{(n)}\left[s\right]$ at $F_g = 0$ is given by

$$\left.\frac{d^2 M^{(2k)}\left[s\right]}{dF^2}\right|_{F_g=0}$$
$$= \int_{-\infty}^{\infty} db\, p_{\rm sl}(b) \left[n(n-1)\left\langle b\right\rangle^2 M^{(n-2)}\left[s|b\right] - \frac{b}{\tilde{\sigma}^2}\left(b + 2n\left\langle b\right\rangle\right) M^{(n)}\left[s|b\right] + \frac{b^2}{\tilde{\sigma}^4} M^{(n+2)}\left[s|b\right]\right].$$

The even moments $M^{(n)}\left[s|b\right]$ of the normal distribution $N\left(s; 0, \tilde{\sigma}^2\right)$ can be expressed as $\tilde{\sigma}^n(n-1)!!$ where $(n-1)!! = (n-1)(n-3)\cdots 3\cdot 1$ is the double factorial. Therefore, we have

$$\left.\frac{d^2 M^{(2k)}\left[s\right]}{dF^2}\right|_{F_g=0} = (n-1)!!\, n \int_{-\infty}^{\infty} p_{\rm sl}(b)\, \tilde{\sigma}^{n-2} \left(b - \left\langle b\right\rangle\right)^2 db > 0$$

for any even n, which implies that $M^{(2k)}\left[s\right]$ indeed achieves its minimum at $F_g = 0$.

References

1. Bloom JS, Ehrenreich IM, Loo WT, Lite TLV, Kruglyak L. Finding the sources of missing heritability in a yeast cross. Nature. 2013;494(7436):234–237.

2. Jerison ER, Kryazhimskiy S, Mitchell JK, Bloom JS, Kruglyak L, Desai MM. Genetic variation in adaptability and pleiotropy in budding yeast. Elife. 2017;6:e27167.

3. Johnson MS, Martsul A, Kryazhimskiy S, Desai MM. Higher-fitness yeast genotypes are less robust to deleterious mutations. Science. 2019;366(6464):490–493.

4. Johnson MS, Desai MM. Mutational robustness changes during long-term adaptation in laboratory budding yeast populations. Elife. 2022;11:e76491.

5. Wrolstad R, Acerr T, Decker E, Penner M, Reid D, Schwartz S, et al. Common buffers and stock solutions. Current Protocols in Food Analytical Chemistry, John Wiley & Sons, Inc. 2001;.

6. Gomori G. Preparation of buffers for use in enzyme studies. Biochemistry and Molecular Biology. 2010; p. 719.

7. Levy SF, Blundell JR, Venkataram S, Petrov DA, Fisher DS, Sherlock G. Quantitative evolutionary dynamics using high-resolution lineage tracking. Nature. 2015;519(7542):181–186.

8. Venkataram S, Kinsler G. BarcodeCounter2; 2021. https://github.com/sandeepvenkataram/BarcodeCounter2.

9. Berger D, Postma E. Biased estimates of diminishing-returns epistasis? Empirical evidence revisited. Genetics. 2014;198(4):1417–1420.

10. Reddy G, Desai MM. Global epistasis emerges from a generic model of a complex trait. Elife. 2021;10:e64740.

2 Supplementary tables

Environment		**Slopes**			**Intercepts**		
Temp, °C	pH	Mean	Stdev	Skew	Mean	Stdev	Skew
30	3.2	−0.109	0.127	−1.492	0.023	0.029	0.724
30	5.0	−0.202	0.185	−1.154	0.059	0.054	0.442
30	7.0	−0.142	0.164	−0.867	0.026	0.035	0.325
37	3.2	−0.133	0.151	−1.015	0.03	0.039	0.45
37	5.0	−0.112	0.162	−0.872	0.025	0.05	0.46
37	7.0	−0.135	0.172	−0.755	0.016	0.036	−0.816

Table S1. Statistics of slope and intercept distributions.

Antibiotic	***E. coli***	***S. cerevisiae***
Kanamycin (Kan)	40	N/A
Ampicilin (Amp)	100	100
Nourseothricin (Nat)	20	20
Hygromycin (Hyg)	200	300

Table S2. Antibiotic concentrations used in this study, in µg/ml.

3 Supplementary figures

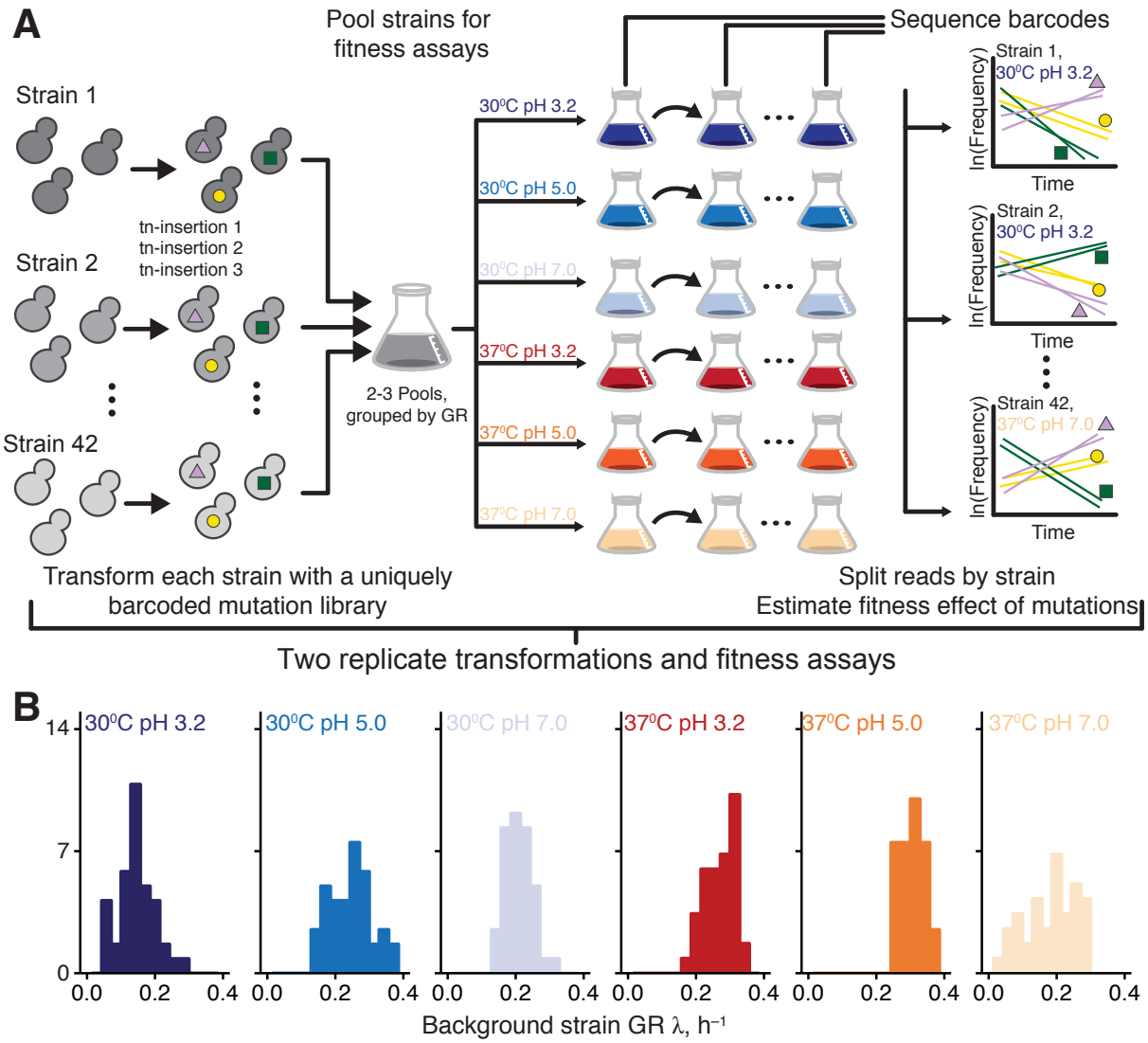

Figure S1. Experimental setup. A. Schematic of the experiment. **B.** Distribution of GRs of background strains in all environments.

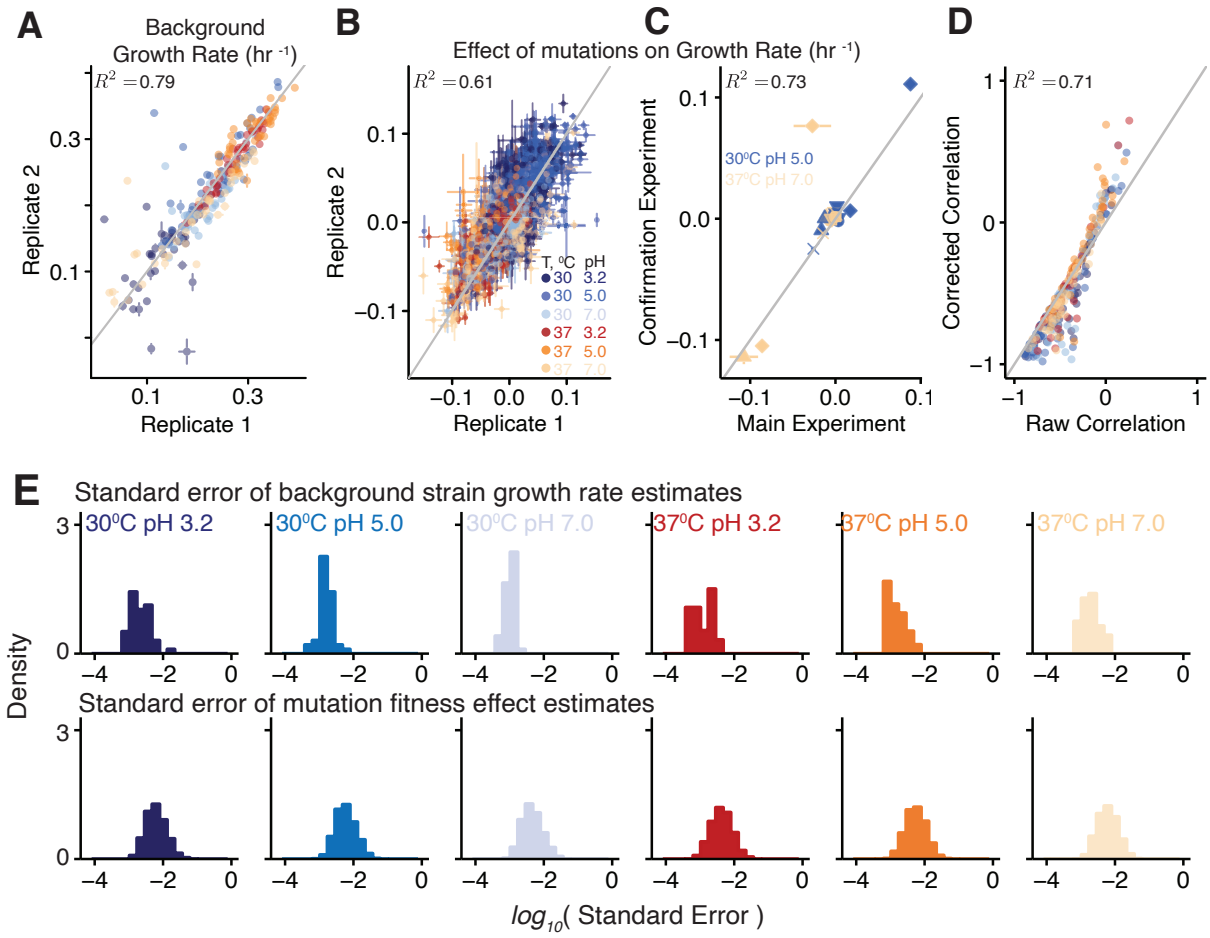

Figure S2. Data quality checks. A. Correlation between GRs of background strains estimated in two biological replicates. **B.** As in panel A, but for the fitness effects of mutations. In both panels, error bars represent ±1 standard error. **C.** Correlation between fitness effect estimates in the high-throughput RB-TnSeq experiment and the validation experiment (see Section 1.2.3). **D.** Raw and corrected estimates of the correlation coefficient between background GR and fitness effect for each mutation in each environment. In all panels, grey line is the diagonal, R^2 is reported for linear regression ($P < 0.01$ for all regressions). **E.** Distribution of the standard error of background strain GRs (top) and mutation effects (bottom) in all environments.

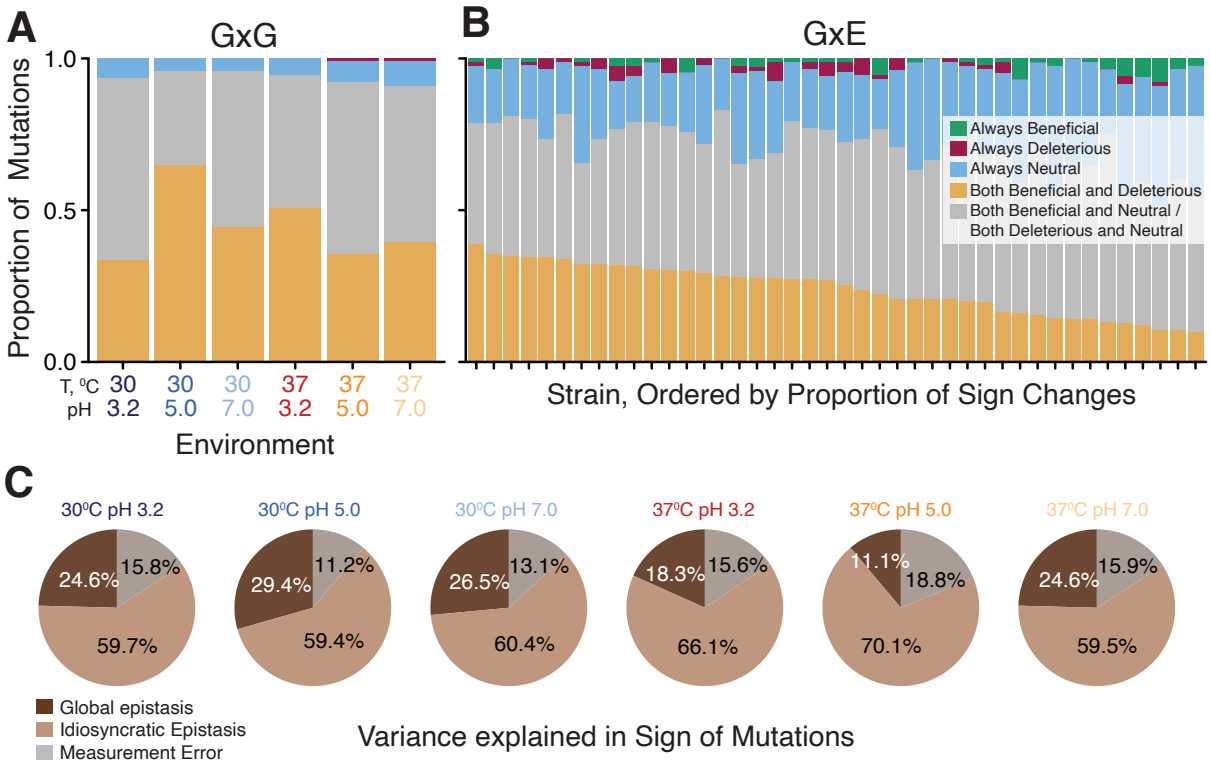

Figure S3. Variation in the sign of mutational effects across genetic backgrounds (G×G interactions) and across environments (G×E interactions). A. Proportions of mutations that do and do not change sign across background strains in each environment. **B.** Proportions of mutations that do and do not change sign across environments in each background strain. **C.** The proportion of variance in the observed sign of mutations in each environment explained by measurement noise, global and idiosyncratic epistasis (see Section 1.3.8 for details).

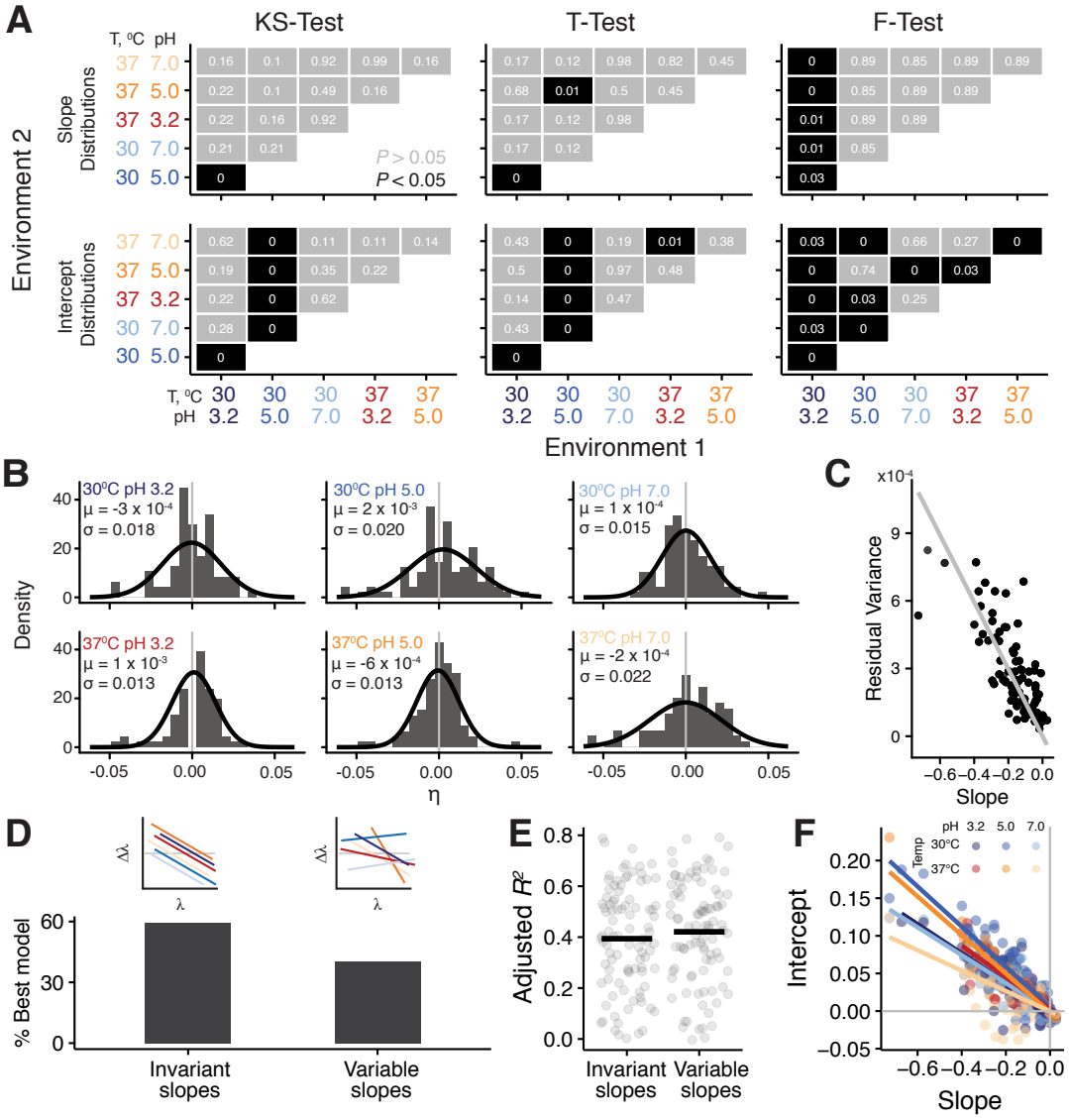

Figure S4. Properties of global epistasis models A. Comparison of distributions of slopes (top) and intercepts (bottom) across environments using three metrics (see Section 1.3.7. The number in each tile is the P-value (after Benjamini-Hochberg correction) of the comparison, and tiles with $P < 0.05$ are colored black. **B.** Distribution of the pivot noise term η in each environment. Mean and variance of the distribution are labelled in each panel, and the best fit normal distribution is overlayed. **C.** Relationship between global epistasis slope and the variance of residuals from the fit of equation (2). Grey line is best fit linear regression through the origin. **D.** Bar graph showing the percent of mutations best fit by the invariant slopes and variable slopes models. Illustrative example of each model is shown on top. **E.** The adjusted R^2 for the fits of both models for all mutations. **F.** Slope intercept correlation for a fit of the invariant slopes model, lines are best fit linear regression through the origin.

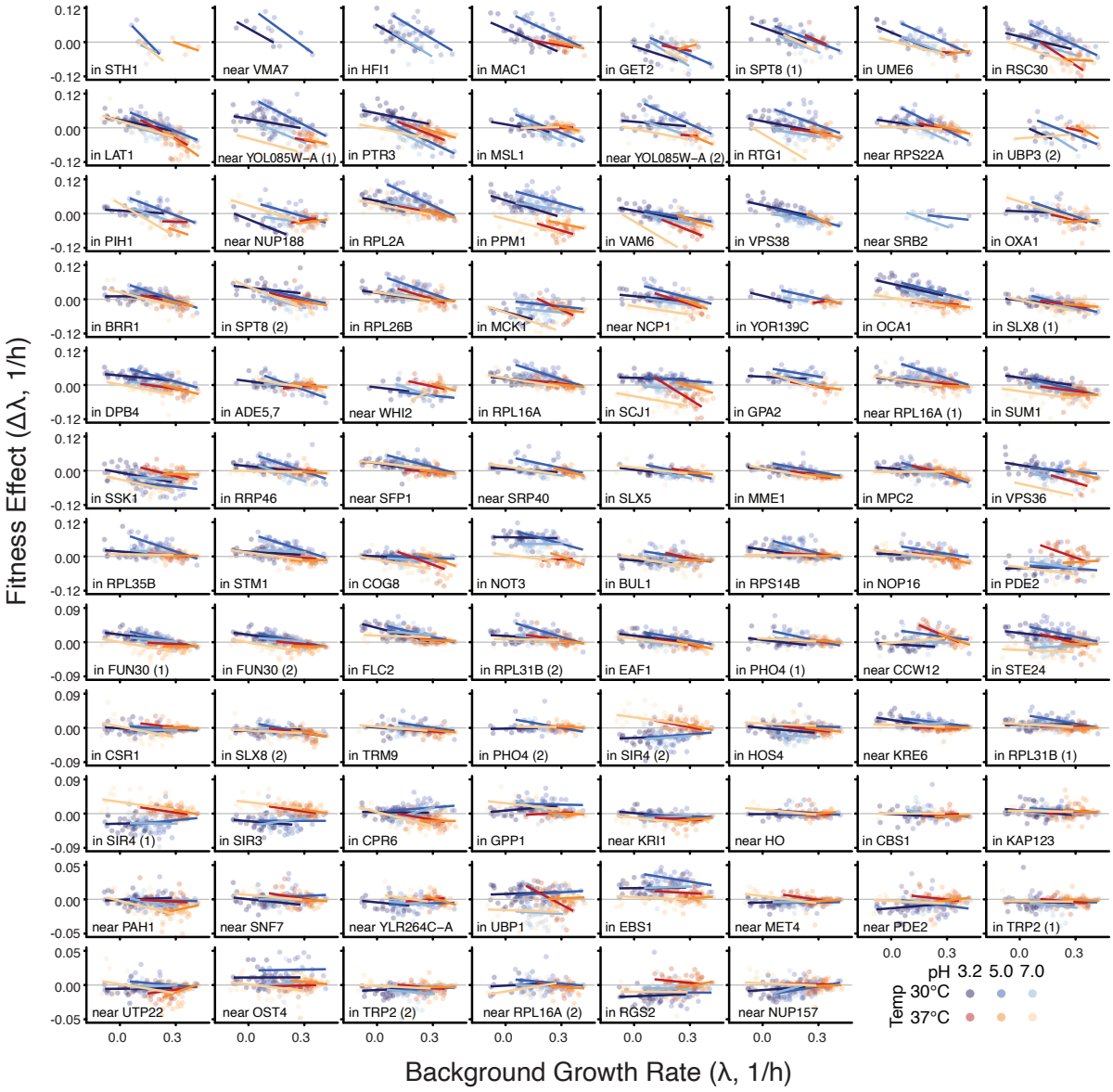

Figure S5. Global epistasis model for individual mutations. Same as Figure 3, but with data points. Mutations are ordered by slope, as in Figure 3. y-axis varies across rows.

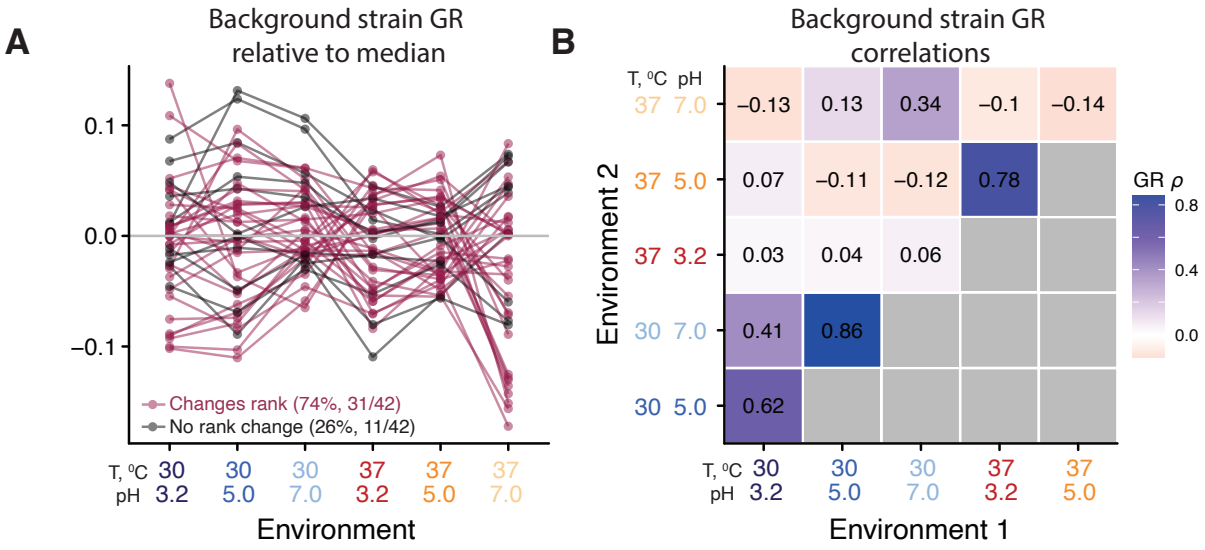

Figure S6. Reshuffling of background strain GRs across environments. A. Strain GR relative to the median GR in each environment. Lines connect the same strain across environments and are colored maroon if the strain is on different sides of the median in different environments. **B.** The correlation of background strain GR across all pairs of environments.

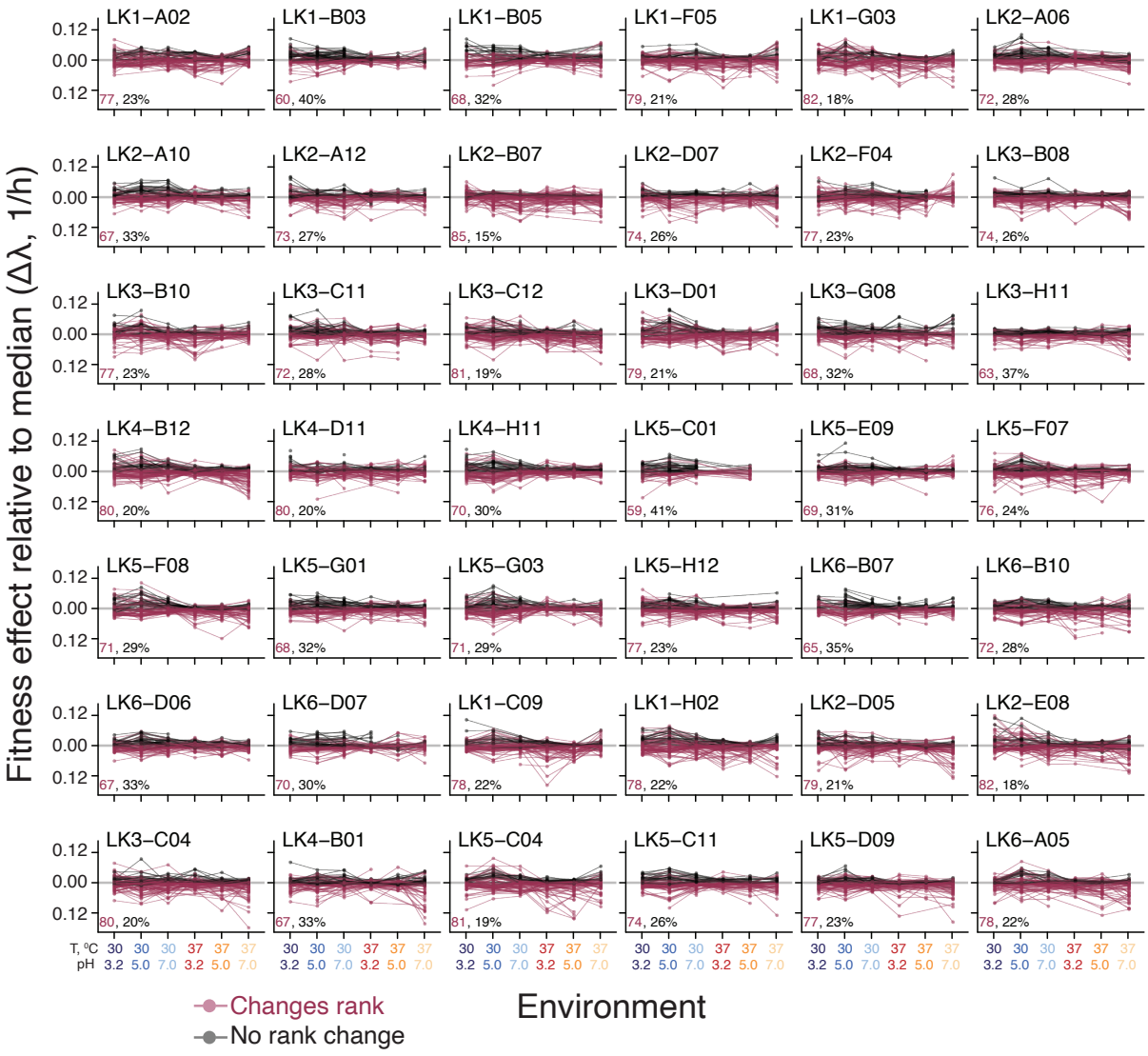

Figure S7. Reshuffling of the effects of mutations across environments. Each panel corresponds to a background strain and shows the effect of all mutations relative to the median in each environment. Lines connect the same mutation across environments and are colored maroon if the mutation is on different sides of the median in different environments.

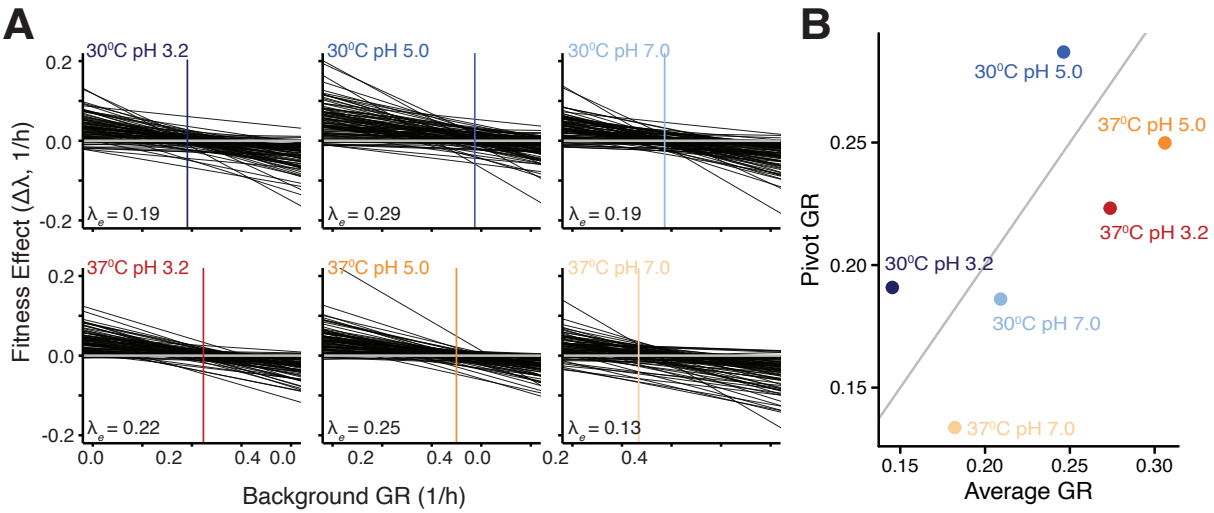

Figure S8. Pivot GRs across environments. A. Best-fit regression lines of the generalized global epistasis equation (2)for all mutations in each environment. Vertical line represents the pivot GR λ_e. **B.** Relationship between the mean background strain GR in each environment and the pivot GR.

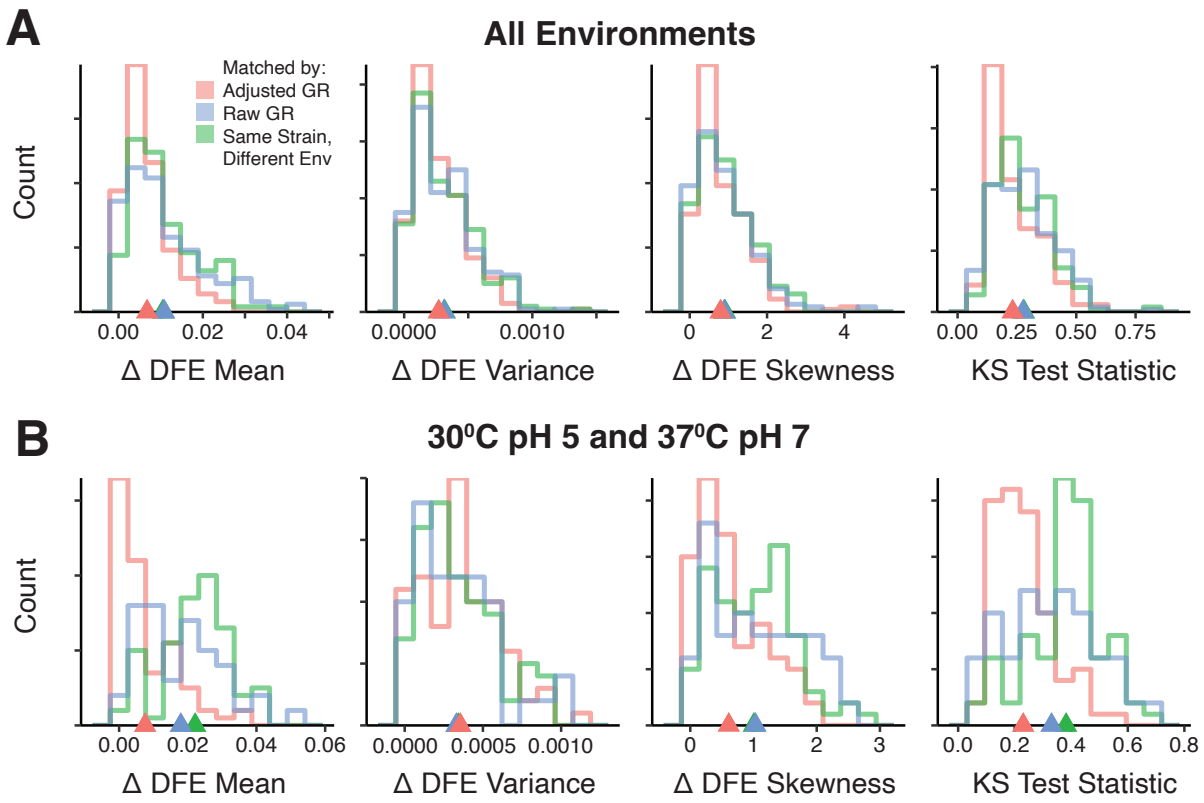

Figure S9. Distributions of DFEs similarity statistics. A. Distribution of four metrics of DFE similarity for all pairs of strains from any two different environments and matched either by their adjusted GR (red), raw GR (blue), or strain identity (green). See Section 1.3.9 for details. For all metrics, lower values mean more similar DFEs. Triangle shows the mean of the corresponding colored distribution. **B.** Same as A but with the strains sampled from the two most dissimilar environments, 30°C pH 5 and 37°C pH 7.

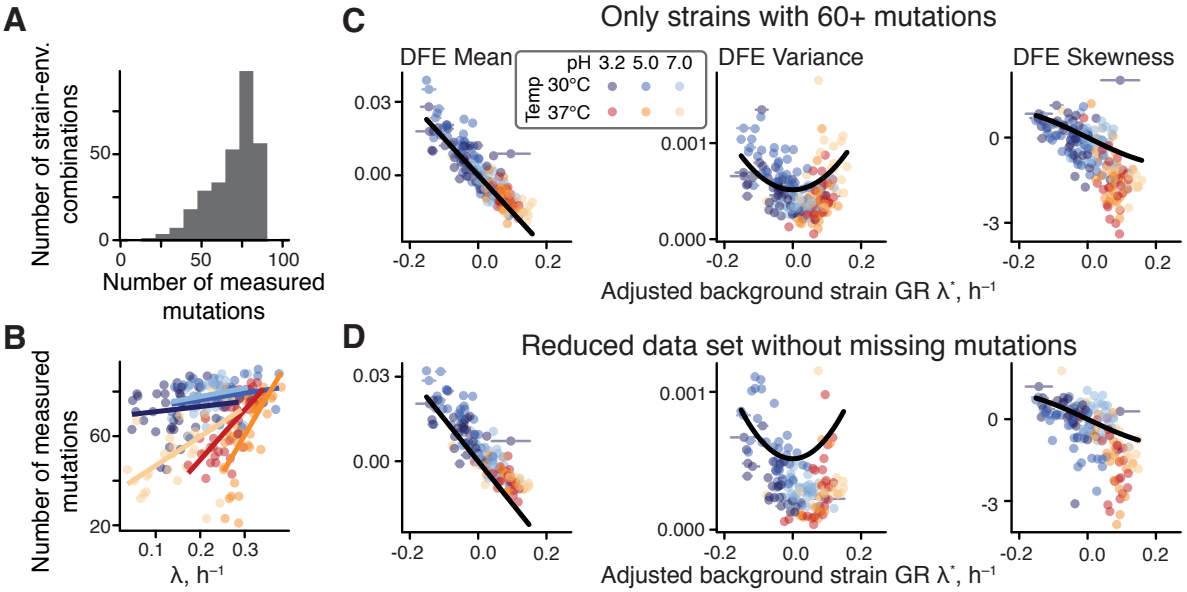

Figure S10. Robustness of the observed DFE variation with respect to missing measurements. A. Distribution of the number of mutations measured per DFE. **B.** Relationship between the number of mutations in each DFE and the background GR. Lines represent the best fit linear regression. **C.** Same as Figure 4 but excluding all strains whose DFE contains less than 60 mutations. **D.** Same as Figure 4 but based on a reduced data set without missing measurements (see Section 1.3.9).

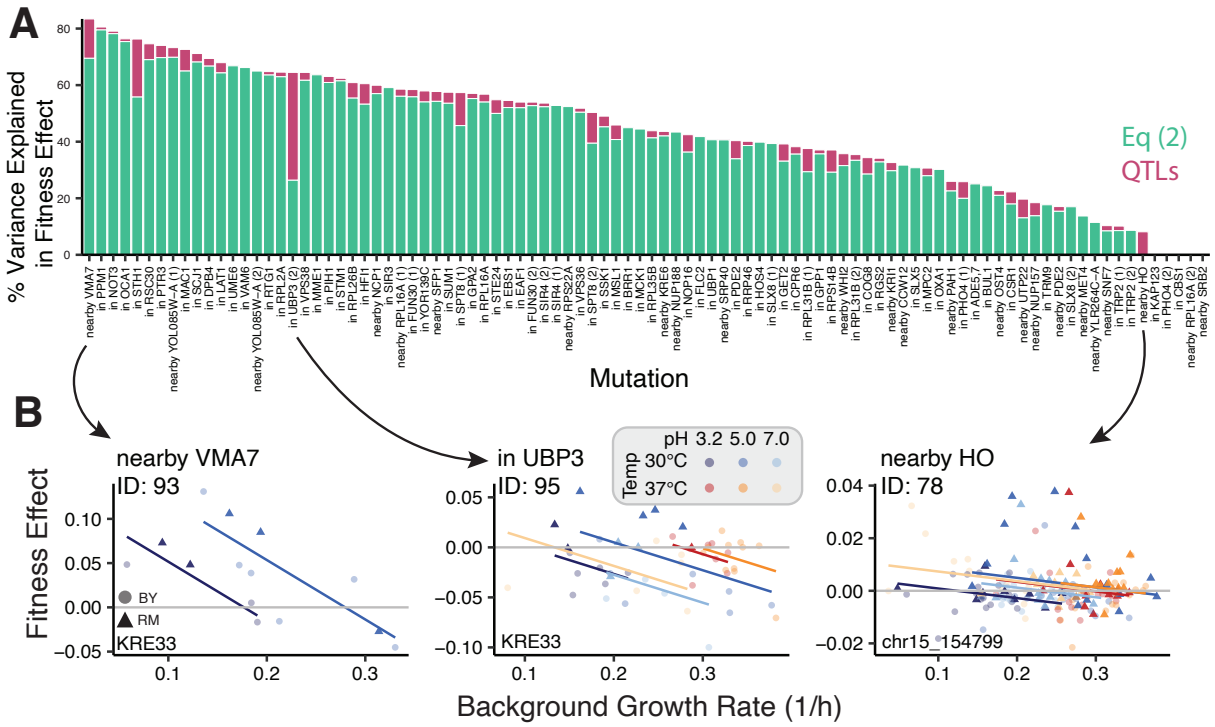

Figure S11. QTL analysis. A. The percent variance in fitness effect of each mutation explained by four candidate loci combined (pink) above and beyond the variance explained by the generalized global epistasis equation (2)(teal). Mutations are ordered by the total explained variance. **B.** Three example mutations, with lines representing the best fit generalized global epistasis model, colored by environment. Point shape represents the allele, either BY (circles) or RM (triangles), at the locus explaining most variation for that mutation (locus indicated in the bottom left of each panel).